On the Use of Field RR Lyrae as Galactic Probes. II. A New ΔS Calibration to Estimate Their Metallicity*

```
J. Crestani<sup>1,2,3</sup>, M. Fabrizio<sup>2,4</sup>, V. F. Braga<sup>2,4</sup>, C. Sneden<sup>5</sup>, G. Preston<sup>6</sup>, I. Ferraro<sup>2</sup>, G. Iannicola<sup>2</sup>, G. Bono<sup>1,2</sup>, A. Alves-Brito<sup>3</sup>, M. Nonino<sup>7</sup>, V. D'Orazi<sup>8,9</sup>, L. Inno<sup>10,11</sup>, M. Monelli<sup>12</sup>, J. Storm<sup>13</sup>, G. Altavilla<sup>2,4</sup>, B. Chaboyer<sup>14</sup>, M. Dall'Ora<sup>10</sup>, G. Fiorentino<sup>2</sup>, C. Gilligan<sup>14</sup>, E. K. Grebel<sup>15</sup>, H. Lala<sup>15</sup>, B. Lemasle<sup>15</sup>, M. Marengo<sup>16</sup>, S. Marinoni<sup>2,4</sup>, P. M. Marrese<sup>2,4</sup>, C. E. Martínez-Vázquez<sup>17</sup>, N. Matsunaga<sup>18</sup>, J. P. Mullen<sup>16</sup>, J. Neeley<sup>19</sup>, Z. Prudil<sup>15</sup>, R. da Silva<sup>2,4</sup>, P. B. Stetson<sup>20</sup>, F. Thévenin<sup>21</sup>, E. Valenti<sup>22,23</sup>, A. Walker<sup>17</sup>, and M. Zoccali<sup>24</sup>
                Dipartimento di Fisica, Università di Roma Tor Vergata, via della Ricerca Scientifica 1, I-00133 Roma, Italy; juliana.crestani@uniroma1.it

2 INAF—Osservatorio Astronomico di Roma, via Frascati 33, I-00078 Monte Porzio Catone, Italy
                 <sup>3</sup> Departamento de Astronomia, Universidade Federal do Rio Grande do Sul, Av. Bento Gonçalves 6500, Porto Alegre 91501-970, Brazil

<sup>4</sup> Space Science Data Center—ASI, via del Politecnico snc, I-00133 Roma, Italy
                                        <sup>5</sup> Department of Astronomy and McDonald Observatory, The University of Texas, Austin, TX 78712, USA
                                      <sup>6</sup> The Observatories of the Carnegie Institution for Science, 813 Santa Barbara St., Pasadena, CA 91101, USA
                                                        INAF—Osservatorio Astronomico di Trieste, Via G.B. Tiepolo 11, I-34143 Trieste, Italy
                                                  8 INAF—Osservatorio Astronomico di Padova, vicolo dellOsservatorio 5, I-35122 Padova, Italy
                                                School of Physics and Astronomy, Monash University, Clayton, VIC 3800 Melbourne, Australia <sup>10</sup> INAF—Osservatorio Astronomico di Capodimonte, Salita Moiariello 1, I-80131 Napoli, Italy
                                         <sup>11</sup> Università Parthenope di Napoli, Science and Technology Department, CDN IC4, I-80143 Naples, Italy
                                                   Instituto de Astrofísica de Canarias, Calle Via Lactea s/n, E-38205 La Laguna, Tenerife, Spain
                                             <sup>13</sup> Leibniz-Institut für Astrophysik Potsdam (AIP), An der Sternwarte 16, D-14482 Potsdam, Germany
                                                         Department of Physics and Astronomy, Dartmouth College, Hanover, NH 03784, USA
               Astronomisches Rechen-Institut, Zentrum für Astronomie der Universität Heidelberg, Mönchhofstr. 12-14, D-69120 Heidelberg, Germany

16 Department of Physics and Astronomy, Iowa State University, Ames, IA 50011, USA
               <sup>17</sup> Cerro Tololo Inter-American Observatory, NSF's National Optical-Infrared Astronomy Research Laboratory, Casilla 603, La Serena, Chile
                                             Department of Astronomy, The University of Tokyo, 7-3-1 Hongo, Bunkyo-ku, Tokyo 113-0033, Japan
             Department of Physics, Florida Atlantic University, 777 Glades Rd, Boca Raton, FL 33431 USA

Department of Physics, Florida Atlantic University, 777 Glades Rd, Boca Raton, FL 33431 USA

Herzberg Astronomy and Astrophysics, National Research Council, 5071 West Saanich Road, Victoria, British Columbia V9E 2E7, Canada
                       Université de Nice Sophia-antipolis, CNRS, Observatoire de la Côte d'Azur, Laboratoire Lagrange, BP 4229, F-06304 Nice, France
                                              European Southern Observatory, Karl-Schwarzschild-Str. 2, D-85748 Garching bei Munchen, Germany
                                                    Excellence Cluster ORIGINS, Boltzmann-Straße 2, D-85748 Garching bei München, Germany
                       <sup>24</sup> Instituto de Astrof\(\frac{1}{2}\)ica Facultad de F\(\frac{1}{2}\)ica, Pontificia Universidad Cat\(\frac{1}{2}\)ica de Chile, Av. Vicu\(\text{i}\)a Mackenna 4860, Santiago, Chile
                                   Received 2020 September 30; revised 2020 November 19; accepted 2020 December 3; published 2021 February 9
```

Abstract

We performed the largest and most homogeneous spectroscopic survey of field RR Lyraes (RRLs). We secured \approx 6300 high-resolution (HR, $R \sim 35,000$) spectra for 143 RRLs (111 fundamental, RRab; 32 first-overtone, RRc). The atmospheric parameters were estimated by using the traditional approach and the iron abundances were measured by using an LTE line analysis. The resulting iron distribution shows a well-defined metal-rich tail approaching solar iron abundance. This suggests that field RRLs experienced a complex chemical enrichment in the early halo formation. We used these data to develop a new calibration of the ΔS method. This diagnostic, based on the equivalent widths of Ca II K and three Balmer $(H_{\delta,\gamma,\beta})$ lines, traces the metallicity of RRLs. For the first time, the new empirical calibration: (i) includes spectra collected over the entire pulsation cycle; (ii) includes RRc variables; (iii) relies on spectroscopic calibrators covering more than three dex in iron abundance; and (iv) provides independent calibrations based on one/two/three Balmer lines. The new calibrations were applied to a data set of both SEGUE-SDSS and degraded HR spectra totalling 6451 low-resolution ($R \sim 2000$) spectra for 5001 RRLs (3439 RRab, 1562 RRc). This resulted in an iron distribution with a median $\eta = -1.55 \pm 0.01$ and $\sigma = 0.51$ dex, in good agreement with literature values. We also found that RRc are 0.10 dex more metal-poor than RRab variables, and have a distribution with a smoother metal-poor tail. This finding supports theoretical prescriptions suggesting a steady decrease in the RRc number when moving from metal-poor to metal-rich stellar environments.

^{*} Based on observations obtained with the du Pont telescope at Las Campanas Observatory, operated by Carnegie Institution for Science. Based in part on data collected at Subaru Telescope, which is operated by the National Astronomical Observatory of Japan. Based partly on data obtained with the STELLA robotic telescopes in Tenerife, an AIP facility jointly operated by AIP and IAC. Some of the observations reported in this paper were obtained with the Southern African Large Telescope (SALT). Based on observations made with the Italian Telescopio Nazionale Galileo (TNG) operated on the island of La Palma by the Fundación Galileo Galilei of the INAF (Istituto Nazionale di Astrofisica) at the Spanish Observatorio del Roque de los Muchachos of the Instituto de Astrofisica de Canarias. Based on observations collected at the European Organisation for Astronomical Research in the Southern Hemisphere.

Unified Astronomy Thesaurus concepts: RR Lyrae variable stars (1410); Milky Way stellar halo (1060); High resolution spectroscopy (2096); Metallicity (1031)

Supporting material: machine-readable tables

1. Introduction

The RR Lyrae (RRL) stars are radially pulsating, core helium burning stars. The fundamental mode and the first-overtone pulsators are categorized as RRab and RRc, respectively, with the RRd being a small population of double-mode pulsators. Being evolved low-mass stars, they are ubiquitous in a variety of environments and cover a wide metallicity range ([Fe/H] ≈ -2.5 to solar). Interestingly, the RRL obey period–luminosity relations in near-infrared bands (e.g., Longmore et al. 1986; Bono et al. 2003, 2019; Braga et al. 2018). These relations make them ideal standard candles, like Cepheids, but with the unique characteristics of tracing necessarily old populations ($\geqslant 10~{\rm Gyr}$) and being very well-studied (e.g., Marconi et al. 2015). Indeed, Classical Cepheids trace exclusively young populations, while Type II Cepheids are old but scarce and still poorly understood (Bono et al. 2020b).

The absolute visual magnitude metallicity relation (Sandage & Tammann 2006) and the period-luminosity relations of the RRLs have made them very popular distance indicators for decades. Field RRLs have also been the focus of several spectroscopic studies (e.g., Preston 1959; Butler et al. 1976, 1979; Saha 1985; Layden 1994, hereafter Layden94), aimed at investigating the early chemical enrichment of both the Halo and the Bulge together with their three-dimensional spatial structure. The question that immediately arises is whether chemical abundance determinations for these stars are reliable across their whole pulsation cycle. After all, even though their short (0.2-1 day) periods make their light curves relatively easy to obtain, the resulting rapid atmospheric changes could make detailed chemical abundance investigations very difficult, in particular for fainter objects. In the past, this difficulty was twofold: first, there was the challenge of observing the star for a sufficiently long time in order to obtain a high signalto-noise ratio (S/N), but not for so long as to cause the smearing of spectral lines due to the varying velocity of the atmospheric layer where the line is formed. Second, it was unclear whether the measured atmospheric metallicity of the RRL remained constant across the pulsation cycle.

The first issue was solved by the development of larger telescopes and increased access to them. Even two-meter class telescopes have great success in obtaining a good S/N in high-dispersion spectrographs for the brighter targets. With eight-meter class telescopes, exposures as short as a few minutes deliver high quality spectra for medium-to-bright targets, allowing a very detailed study of the atmospheric phenomena in these stars (Chadid et al. 2008; Gillet et al. 2016). As for the second issue, breakthroughs came with the works of For et al. (2011) for the RRab and Sneden et al. (2017) for the RRc, both of which demonstrated that the observed metallicity of RRL remain constant within uncertainties for the entire pulsation cycle. The same result has been found by Magurno et al. (2019) for a large sample of RRL in the ω Centauri globular cluster (GC).

These developments confirmed that coherent chemical abundance results can be recovered during the whole pulsation cycle, thus opening the door for random phase observations. This efficient approach to observations caused a significant increase in the number of RRL with spectroscopic studies. Indeed, with the

nonlinear effects caused by shockwaves being restricted to a narrow phase window, a series of observations of any given RRL can easily provide perfectly usable data. However, high-resolution (HR) spectroscopy is still a resource-consuming endeavor. A single RRL is capable of constraining both chemical abundance and distance, yet a detailed study of a stellar population requires a large number of such observations. It is still unviable to acquire high-dispersion spectra for objects beyond the Milky Way, or to obtain and analyze a very large number of such spectra in order to perform detailed studies of the Galactic halo. Both stellar distance and sample size are strong constraints on the applicability of HR spectroscopy.

Originally, the ΔS method consisted of deriving two spectral types for a given RRL, one only considering the Balmer series features $(H_{\beta}, H_{\gamma}, H_{\delta})$ and the other only the Ca II K line. The difference in spectral type between these two indicators was then associated with a difference in metallicity (Preston 1959; Butler 1975). Following this working hypothesis, the studies of Freeman & Rodgers (1975), Suntzeff et al. (1991), and Layden (1994) demonstrated that the equivalent widths of the Ca II K and three of the Balmer series features can also be associated with the metallicity of a given RRL without the use of the spectral type. These features are extremely strong and can be reliably measured at very low spectral resolutions. This means that, once a calibration using high-dispersion spectroscopy is derived, low-resolution (LR) measurements are sufficient to provide metallicity estimates. This equivalent-width approach is the basis of the ΔS method as it is discussed in the present work.

The ΔS method is behind the majority of metallicity estimates of RRL stars in the literature directly, via its application to LR spectra, or indirectly, when its results are used to calibrate other metallicity indicators such as the Fourier parameter decomposition method. This LR spectroscopic metallicity indicator is an approach that balances the precision of HR spectroscopy with the efficiency of photometry. Wallerstein et al. (2012) have adapted the ΔS method to use the infrared Ca II line at 8498 Å covered by the Gaia spectrograph (Cropper et al. 2018). Another related method using the Ca II K line and the Balmer series features was employed by Liu et al. (2020), using synthetic spectra matching instead of equivalent widths.

The calibration provided by Layden94 is widely used in the literature (Dambis et al. 2013), although later ones exist (e.g., Gratton et al. 2004). It was produced using 19 RRab stars at minimum light phases and applied a metallicity scale transformation based on seven GCs to provide values in the Zinn & West (1984) scale. In this work, we employed the largest and most homogeneous HR spectroscopic sample of field RRL stars ever used in the literature, to provide a brandnew calibration of ΔS method across the entire pulsation cycle for both RRab and RRc stars, including in the metal-rich and metal-poor tails that were previously poorly sampled.

Our sample allows us to both determine the metallicities in HR in a homogeneous way and to obtain the ΔS measurements once the spectra were downgraded to LR. With this, this new calibration makes use of no metallicity scale transformations.

 Table 1

 Identification, Photometric Characteristics, Classification, and Number of Spectra for the CHR

GaiaID (DR2)	Star	R.A. _{J2000} (deg)	Decl. _{J2000} (deg)	Vmag (mag)	Vamp (mag)	P (day)	Class	Blazhko	N Spectra
4224859720193721856	AA Aql	309.5628	-2.8903	11.86	1.16	0.36	RRab	?	1
2608819623000543744	AA Aqr	339.0161	-10.0153	12.93	0.99	0.61	RRab	?	1
1234729400256865664	AE Boo	221.8968	16.8453	10.62	0.45	0.31	RRc	?	5
3604450388616968576	AM Vir	200.8889	-16.6663	11.45	0.69	0.62	RRab	Yes	141
1191510003353849472	AN Ser	238.3794	12.9611	10.92	1.01	0.52	RRab	No	67

(This table is available in its entirety in machine-readable form.)

As we have dozens of calibrating stars, anyone who wishes to perform new measurements in our system has several good reference targets to choose from. This means no equivalent width system transformations are necessary either. Moreover, we streamlined some features of the IDL code EWIMH, 25 one of several codes traditionally employed for the ΔS measurements, to make full use of the much higher-quality spectrographs currently in use. These changes are easy to implement in other codes for the same purpose.

This paper is organized as follows. In Section 2, we describe the spectroscopic data sets, and in Section 3, how they are organized into samples. In Section 4, we discuss the changes made to the definition of the ΔS method, as well as the changes to how the measurements are performed by the code. The calibration between the ΔS index and [Fe/H] is provided in Section 5. In Section 6, we compare our results with the literature in both HR and LR. Finally, in Section 7, the calibration is applied to a large sample of field RRLs, including hundreds of RRc and one RRd. A summary and final remarks are given in Section 8. In Appendix A, we further discuss the differences between the current calibration and Layden94, and we present some considerations with regard to phase. Throughout this work, we employ the letter η to refer to the median values of whatever quantity is being discussed, e.g., the median of a distribution or the median of the residuals in consideration.

2. Spectroscopic Data Sets

To provide firm constraints on the metallicity distribution of the Galactic halo, we adopted the same photometric catalog built in F19, the first paper of this series. To take into account new optical RRL catalogs and surveys that have been recently published, the original photometric catalog was complemented with four new data sets provided by Catalina (Drake et al. 2017), PANSTARRS (Sesar et al. 2017), ASA-SN (Jayasinghe et al. 2019), and DECAM (Stringer et al. 2019). The selection criteria are the same discussed in F19. The new final photometric catalog includes ~179,000 RRLs and was the starting point for collecting the spectroscopic data set. A detailed description of the construction of this catalog is provided in a companion paper (V. F. Braga et al. 2021, in preparation).

2.1. HR Spectroscopic Data Set

We have collected a sample of 6631 spectra for 266 stars (173 RRab, 92 RRc, and 1 RRd; see Table 1) across the pulsation phase from multiple medium and HR spectrographs. The largest and most homogeneous subsample was collected with the echelle

spectrograph at du Pont (Las Campanas Observatory) and includes 6070 HR (R = 35,000) spectra of 186 RRL (107 RRab, 79 RRc). It typically covers wavelengths from 3600 to 9300 Å.

These data were complemented with 530 optical spectra from the ESO Archive. We included spectra from UVES and X-shooter at VLT (Cerro Paranal Observatory), HARPS at the 3.6 m telescope (La Silla Observatory), and FEROS at the 2.2 m telescope (La Silla Observatory). An additional ten spectra were added from HARPS-N at the Telescopio Nazionale Galileo (Roque de Los Muchachos Observatory), along with four from HRS (Crause et al. 2014) at SALT (South African Astronomical Observatory), six from the HDS (Noguchi et al. 2002) at Subaru (National Astronomical Observatory of Japan), and eleven from the echelle spectrograph (Weber et al. 2012) at STELLA (Izana Observatory). Typical spectra for all spectrographs can be seen in Figure 1.

The distribution of exposure times peaks at \approx 400 s, with an average 434 s, and standard deviation 303 s. The reddening-and distance-independent photometric characteristics of the ΔS calibrating sample, discussed in greater detail in Section 3, are shown in Figure 2. Visual magnitudes and amplitudes were derived from Gaia *G*-band observations using the *V*-band transformation provided by Evans et al. (2018). We also collected native *V*-band photometry from ASAS (Pojmanski 2002), ASAS-SN (Shappee et al. 2014; Jayasinghe et al. 2018), and Catalina (Drake et al. 2013a, 2013b; Torrealba et al. 2015).

The normalizations and Doppler shift corrections were computed and applied using the National Optical Astronomy Observatory libraries for IRAF²⁶ (Image Reduction and Analysis Facility; Tody 1993). In-depth information regarding the radial velocity studies and phasing applied to this same sample can be found in Bono et al. (2020a).

It is important to note that automatic continuum normalization methods must be employed with caution. Using high-order functions to fit the continuum may result in the Ca II K and H lines being made significantly shallower than they truly are. This can occur in spectrographs where the continuum emission in each echelle order is not very smooth and requires higher-order fitting functions. For the du Pont sample, due to its large size, we developed an algorithm that used the smoothest echelle orders neighboring the order where the line of interest was present. These neighbor orders, devoid of any strong absorption features, were used to determine the best continuum fit, which was then applied to the order of interest.

All HR spectra that displayed measurable Ca II K and at least one Balmer hydrogen line (H_{δ}, H_{γ}, H_{β}) were downgraded to R = 2000 for the measurement of the equivalent widths

²⁵ The code and documentation can be found at http://physics.bgsu.edu/~layden/ASTRO/DATA/EXPORT/EWIMH/ewimh.htm.

²⁶ The legacy code is now maintained by the community on GitHub at https://iraf-community.github.io/.

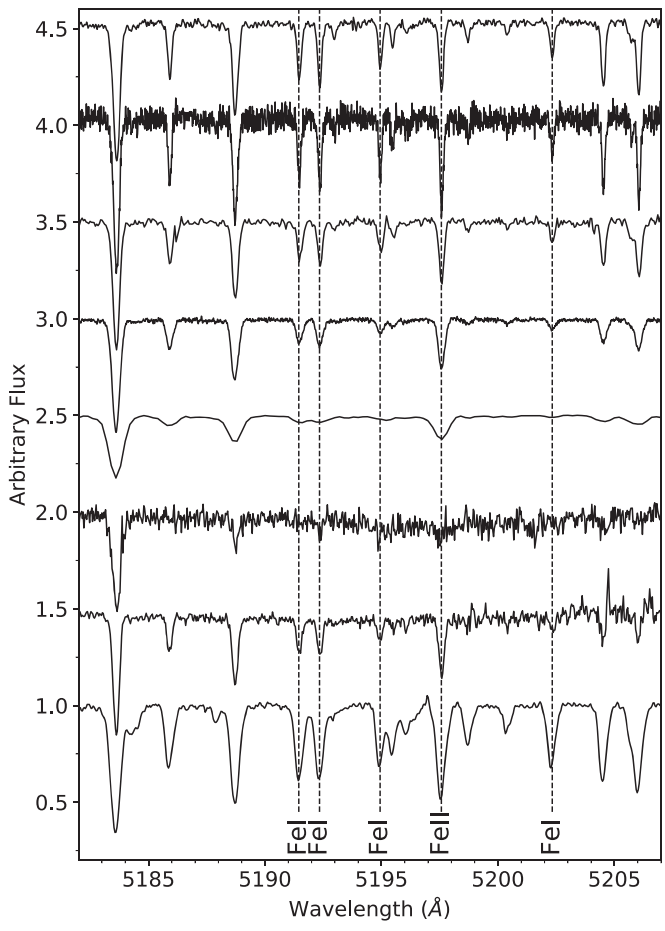


Figure 1. Examples of high-resolution spectra from all spectrographs used in this work. From top to bottom: FEROS, HARPS, du Pont, UVES, X-shooter, Subaru HDS, STELLA, and SALT. The first five spectra are of V Ind ([Fe/H] = -1.63 ± 0.03) near phase 0.40. They are followed by random phase spectra for X Ari ([Fe/H] = -2.59 ± 0.05), DH Peg ([Fe/H] = -1.37 ± 0.05), and RW Tra ([Fe/H] = 0.13 ± 0.06). Dashed lines indicate the strongest iron lines present in this wavelength region.

necessary for the application of the ΔS method (Section 4). Spectra of stars for which we have HR metallicity measurements from this work or For et al. (2011), Chadid et al. (2017), and Sneden et al. (2017), hereafter cited together as For +Chadid+Sneden, form the calibrating sample. The rest were downgraded and rebinned to LR and included in the LR sample. Both samples are described in Section 3.

2.2. LR Spectroscopic Data Set

We took advantage of the huge LR ($R \approx 2000$) spectroscopic data set collected by the Sloan Extension for Galactic Exploration and Understanding Survey of the Sloan Digital Sky Survey (SEGUE-SDSS; Yanny et al. 2009), with the 2.5 m Sloan Foundation Telescope at the Apache Point Observatory. The selection criteria for the spectroscopic sample were already discussed in detail in the first paper of this series (Fabrizio et al. 2019, hereafter F19). Note that the F19 investigation was only based on fundamental RRLs, so in the present work, the RRc are added for the first time.

Most stars in the SEGUE-SDSS sample have only one or two exposures. To apply the new ΔS calibration, we selected

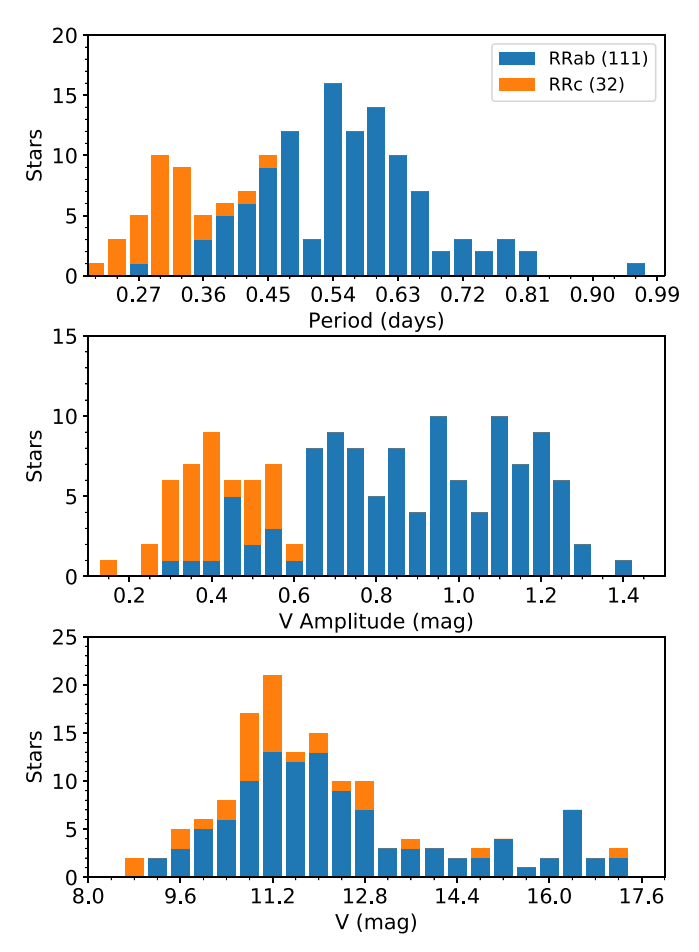


Figure 2. Period (top), visual amplitude (middle), and apparent visual magnitude (bottom) distributions for the RRab (blue) and RRc (orange) in the calibrating sample.

spectra with S/N greater than 15, as well as those that had S/N smaller than 15 but passed a visual inspection. The inspection was performed individually in order to assess the quality of the Ca $\rm II~K$ and Balmer lines. We ended up with a sample of 6299 spectra for 4883 stars, of which 3379 are RRab and 1504 are RRc.

3. RR Lyrae Spectroscopic Samples

The 143 stars (111 RRab, 32 RRc) for which we have HR metallicity measurements either from this work or from For +Chadid+Sneden, and which also have ΔS measurements in the new definition, were included in the calibrating sample (CHR). Those, together with 67 stars (59 RRab, 8 RRc) with HR measurements in the literature that could be brought onto our scale, were included in the HR sample. Finally, the LR sample contains 5001 stars (3439 RRab, 1562 RRc) for which HR estimates were not available. Each sample is discussed in greater detail below.

3.1. HR Calibrating Sample

HR metallicities were derived from 171 measurements of 111 calibrating stars (91 RRab, 20 RRc; see Table 2). Wherever possible, we analyzed two exposures per star. In cases where there were no spectra with high enough S/N for

Table 2

Atmospheric Parameters Derived in This Work for Each Individual Measurement

GaiaID (DR2)	Star	Class	Spectrograph	T _{eff} (K)	$\log(g)$ (dex)	(km s^{-1})	[Fe I/H] (dex)	N _{Fe I}	[Fe II/H] (dex)	N _{Fe II}
4224859720193721856	AA Aql	RRab	SALT	6610 ± 65	2.70 ± 0.01	2.52 ± 0.04	-0.34 ± 0.24	206	-0.34 ± 0.22	39
2608819623000543744	AA Aqr	RRab	UVES	5840 ± 80	1.52 ± 0.06	3.51 ± 0.13	-2.31 ± 0.10	37	-2.31 ± 0.12	13
1234729400256865664	AE Boo	RRc	HARPS	6630 ± 75	2.04 ± 0.04	2.79 ± 0.05	-1.62 ± 0.14	64	-1.62 ± 0.10	25
3604450388616968576	AM Vir	RRab	DuPont	5870 ± 50	1.52 ± 0.06	3.32 ± 0.06	-1.70 ± 0.13	87	-1.70 ± 0.17	25
3626569264033312896	AS Vir	RRab	DuPont	6030 ± 75	1.66 ± 0.10	3.44 ± 0.11	-1.80 ± 0.14	38	-1.80 ± 0.22	12

(This table is available in its entirety in machine-readable form.)

 Table 3

 List of Fe I and Fe II Lines Adopted in This Work for the Determination of Atmospheric Parameters

Wavelength (Å)	Species	EP (eV)	$\log(gf)$ (dex)	Source
3763.78	26.0	0.989	-0.220	OBR91
3787.88	26.0	1.010	-0.840	OBR91
3815.84	26.0	1.484	0.240	OBR91
3820.42	26.0	0.858	0.160	OBR91
3825.88	26.0	0.914	-0.020	OBR91

Note. References: (1) Bard et al. 1991 (BAR91); Bard & Kock 1994 (BAR94); Belmonte et al. 2017 (BEL17); Blackwell et al. 1979 (BLA79); Blackwell et al. 1982 (BLA82); Blackwell et al. 1986 (BLA86); Bridges & Kornblith 1974 (BRI74); Den Hartog et al. 2014 (DEN14); Kock et al. 1984 (KOC84); Den Hartog et al. 2019 (LAWLER); May et al. 1974 (MAY74); Meléndez & Barbuy 2009 (MELBAR); O'Brian et al. 1991 (OBR91); Ruffoni et al. 2014 (RUF14). The prefix NIST denotes the line has had its transition parameters updated by NIST.

(This table is available in its entirety in machine-readable form.)

abundance analysis (S/N \gtrsim 50), we stacked spectra obtained at the same pulsation phase. The method for the determination of the pulsation periods for the whole sample is described in Bono et al. (2020a). Unlike the aforementioned work, however, we have defined the initial point of the pulsation cycle, i.e., phase zero, as the point where the magnitude along the decreasing branch of the light curve is equal to the mean magnitude of the variable (Braga et al. 2016). This initial point, also called the reference epoch, is arbitrary and only moves the light and velocity curves rigidly alongside the phase axis.

When stacking spectra, it is essential to make sure that all stacked spectra were collected at times where the stellar atmosphere had nearly the same thermodynamical configuration. Both observations (For et al. 2011) and theoretical models (Bono & Stellingwerf 1992) show that the atmospheres of RRL stars undergo temperature changes as large as 1000 K. The clearest sign of different atmospheric temperatures between two spectra is a difference between the strength of the absorption lines, as well as their profiles. At lower temperatures, metallic lines are deeper and display larger EWs, while hydrogen lines are shallower and have smaller EWs.

With this in mind, when stacking spectra, we performed a phase selection as a first criterion. This ensures that the spectra were collected when the star was in the same moment of its pulsation cycle. Afterward, we visually inspected all spectra to be stacked in order to verify they showed similar equivalent widths and profiles for the same lines. Verifying the equivalent widths guarantees that all combined spectra were collected roughly at the same pulsation phase. With this conservative approach, any precision concerns with the phasing do not affect the quality of the stacking. Furthermore, any possible issues

with the rest-frame velocity correction are detected at this point in case the central wavelengths of absorption features fail to align. This visual inspection avoids the artificial line smearing caused by stacking spectra where the Doppler shift has not been properly accounted for.

We built a line list of of 415 Fe I and 56 Fe II lines with the most up-to-date transition parameters found in the literature, with a preference for laboratory values. The parameters and references are presented in Table 3. The lines with a reference that begin with the prefix NIST have updated transition parameters taken from the National Institute of Standards and Technology (NIST) Atomic Spectra Database. The list was carefully cleaned of blended lines using both the Moore et al. (1966) solar spectrum atlas and synthetic spectra as a reference. The average number of usable lines in each spectrum was 66 for Fe I and 19 for Fe II (Figure 3).

Equivalent widths were measured manually using the IRAF task SPLOT to perform a Gaussian fit of the core of each line. There were no strong line asymmetries in any of the spectra used for this purpose. We performed an LTE line analysis using the 2019 release of MOG²⁸ (Sneden 1973) paired with an interpolated grid of α -enhanced ATLAS9 model atmospheres (Castelli & Kurucz 2003). Thus, we constrained the atmospheric parameters (effective temperature $T_{\rm eff}$, surface gravity $\log(g)$, metallicity [Fe/H], and microturbulent velocity $\xi_{\rm t}$) using the traditional approach, i.e., iteratively changing their values until achieving excitation equilibrium of Fe I lines, ionization equilibrium of Fe I and Fe II lines, and no trend

²⁷ Available at https://www.nist.gov/pml/atomic-spectra-database.

²⁸ The code and documentation can be found at https://www.as.utexas.edu/~chris/moog.html.

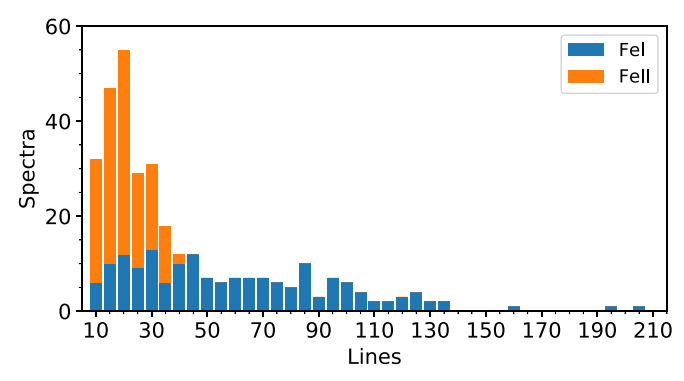


Figure 3. Distribution of the number of adopted Fe I (blue) and Fe II (orange) lines per spectrum. A total of 174 spectra of 111 stars (91 RRab, 20 RRc) were used.

Table 4
[Fe/H] Shifts Required to Bring the Literature Values to our Scale

Source	N	Δ	σ
A18	12	-0.06	0.20
C95	6	-0.14	0.12
F96	2	-0.06	0.09
G14	8	0.21	0.16
L13	12	-0.24	0.12
L96	9	-0.06	0.13
N13	5	-0.15	0.20
P15	10	-0.24	0.14
Total	64	-0.11	0.20

Note. The number of stars in common is denoted by N, the median residuals by Δ , and their standard deviation by σ . To bring metallicity values from these works into our scale, the shift Δ must be added to them after they are put in the Asplund et al. (2009) solar scale. References: (1) Andrievsky et al. 2018 (A18); (2) Clementini et al. 1995 (C95); (3) Fernley & Barnes 1996 (F96); (4) Govea et al. 2014 (G14); (5) Liu et al. 2013 (L13); (6) Lambert et al. 1996 (L96); (7) Nemec et al. 2013 (N13); Pancino et al. 2015 (P15).

between the abundances of Fe I lines and their reduced equivalent widths.

The final metallicity value for each star was taken as the simple mean of all its measurements. When more than one measurement was available for a given star, the uncertainty was taken to be the standard deviation of these measurements. This allowed us to compute a typical [Fe/H] uncertainty for each spectrograph by taking the median of these values for each instrument. This spectrograph-based median uncertainty was then adopted for the stars with a single spectrum, indicated by an asterisk on the last column of Table 4.

The median standard deviations for the uncertainties of the atmospheric parameters are $\sigma(T_{\rm eff}) = 150 \pm 136~{\rm K}$, $\sigma(\log(g)) = 0.43 \pm 0.16~{\rm dex}$, and $\sigma(\xi_{\rm t}) = 0.14 \pm 0.25~{\rm km~s^{-1}}$. To compute the impact of these values in the metallicity estimates, we have applied them to V Ind. We changed the temperature by 150 K while keeping the other parameters in their final adopted value, and we registered the difference $\Delta[{\rm Fe/H}]_{T_{\rm eff}}$ for Fe I and Fe II lines that this change created. We did the same for $\log(g)$ and $\xi_{\rm t}$, changing one parameter at a time and keeping the other parameters at their final value. Finally, we added in quadrature the three values of $\Delta[{\rm Fe/H}]$ for Fe I and three for Fe II. This resulted in a difference of 0.11 for Fe I and 0.14 for Fe II when compared to the final adopted atmosphere. Note that we show

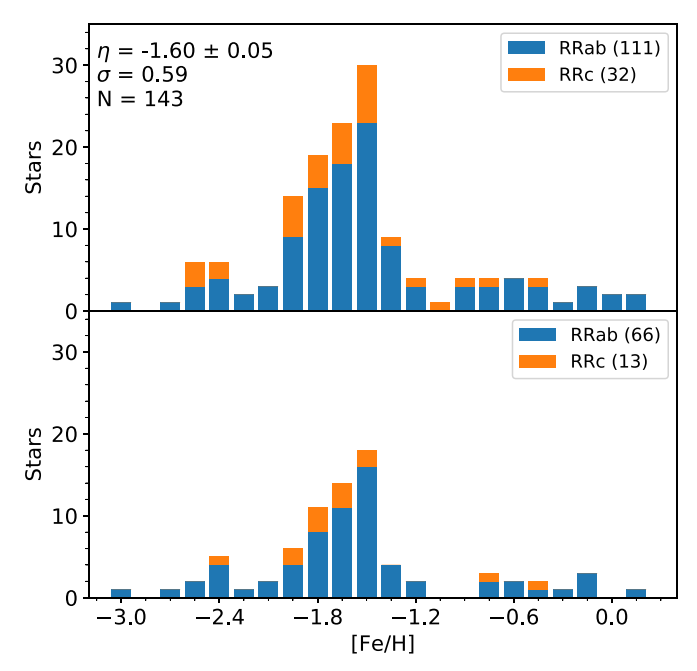


Figure 4. Top: metallicity distribution of the 143 calibrating RRLs (RRab in blue, RRc in orange) based on high-resolution spectra. These include new homogeneous measurements for 32 stars with previous measurements in the literature, along with the results provided by For+Chadid+Sneden for another 32 stars. Bottom: same as the top, but considering only the 79 stars for which we have provided high-resolution metallicities for the first time.

these values for reference only. The reason is that the sum in quadrature of correlated errors overestimates the final error, while it also does not take systematics into account. The metallicity errors derived by the standard deviation from multiple measurements of the same star are therefore a more robust uncertainty indicator, and that is the value we have adopted, as described in the previous paragraph.

HR metallicities for an additional 32 stars (20 RRab, 12 RRc) were collected from three previous works using part of the Du Pont subsample (For+Chadid+Sneden). All their uncertainties are the standard deviation derived from multiple metallicity estimates in the same work. Stars with fewer than two measurements were not considered. The final adopted mean metallicities and their uncertainties are listed in Table 4. The estimates from the present work and of these three sources can be treated as a single homogeneous sample and produce a metallicity distribution ranging from -3.0 to 0.2 (Figure 4). Thus, the entire metallicity range of RRL stars is covered in our calibrating sample of 143 RRL (111 RRab, 32 RRc).

In order to validate our HR measurements, we have compared them to all other such measurements for the same stars in the literature. This comparison is shown in Figure 5, with the references listed in Table 5.

3.2. HR Sample

In addition to the sample described above, we derived metallicities for a mixed-mode pulsator from a total of ten X-shooter and two FEROS spectra individually, i.e., without stacking. It was not included in the CHR sample, because we aimed to verify whether a mixed-mode pulsator would respond coherently to a ΔS calibration made from a sample of both RRab and RRc.

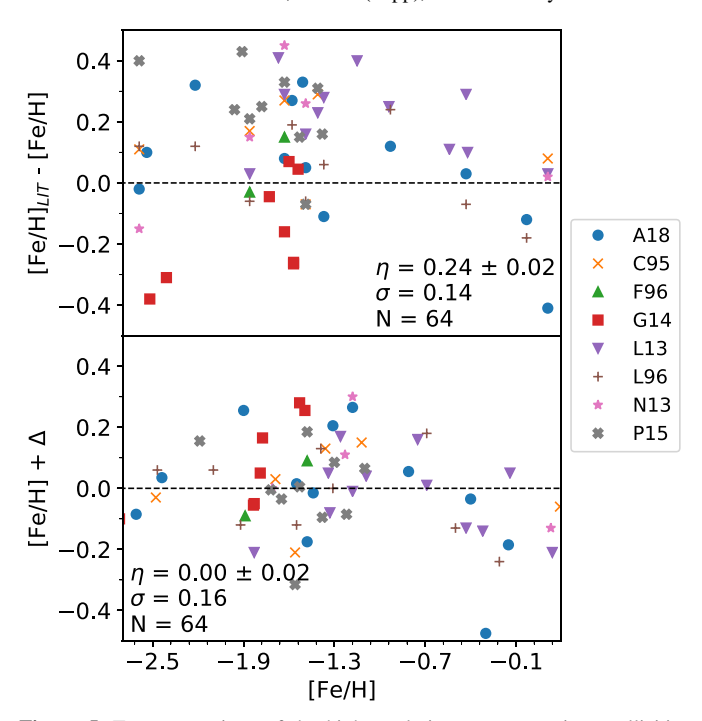


Figure 5. Top: comparison of the high-resolution spectroscopic metallicities adopted in this work with those available in the literature, transformed to the Asplund et al. (2009) solar scale. Bottom: the same comparison once the shift Δ is applied to the literature values, bringing them to our scale. References and shifts are listed in Table 4.

 Table 5

 Adopted Metallicities and Uncertainties for the Stars in the CHR Sample

GaiaID (DR2)	Star	Class	[Fe/H] (dex)	Source
4224859720193721856	AA Aql	RRab	-0.42 ± 0.11	1
2608819623000543744	AA Aqr	RRab	-2.31 ± 0.04	1*
1234729400256865664	AE Boo	RRc	-1.62 ± 0.09	1*
3604450388616968576	AM Vir	RRab	-1.77 ± 0.09	1
1191510003353849472	AN Ser	RRab	0.05 ± 0.01	4

Note. References. (1) This work; (2) For et al. 2011; (3) Sneden et al. 2017; (4) Chadid et al. 2017. An asterisk denotes that the value was derived from a single measurement, and the uncertainty from the typical instrumental uncertainty. See text for details.

(This table is available in its entirety in machine-readable form.)

A total of 134 field RRL have HR iron abundance estimates in the literature. Among these, 64 stars in eight studies are in common with our CHR sample, while two were in a study without any overlap with this work and thus were neglected. This allowed us to compute the shifts that need to be added to eight studies in order to bring their metallicity results into our scale (Figure 5, Table 4). We have applied these shifts to another 67 stars that were in these studies, for which we have no metallicity estimate of our own. With the shifts applied, these 67 stars, alongside the CHR sample and the RRd mentioned above, form the HR sample with a total of 211 stars (170 RRab, 40 RRc, 1 RRd). It is the largest, most homogenous sample of HR metallicity measurements of field RRL stars. Indeed, it is almost a factor of two larger than any previous data sets of the same type in the literature (Magurno et al. 2018, 2019).

3.3. LR Sample

Together with the spectra used for the CHR sample, we have had at our disposal another 298 HR spectra of 121 stars (62 RRab, 59 RRc). They were not included among the calibrating RRLs, because they had low S/N and were collected at different phases, making spectra stacking unviable. We degraded and rebinned their spectra to a spectral resolution $R \approx 2000$ and sampling $\Delta \log(\lambda) = 0,0001$, in order to mimic the native resolution of the SEGUE-SDSS spectra. This increased their S/N by a factor of four to five, approximately. Each star has its own individual $[Fe/H]_{\Delta S}$ computed in the same way the values for the CHR sample were computed (Section 5). None of these stars has HR metallicity measurements in the literature.

The main reason why we developed a new ΔS calibration is to apply it to LR spectra. Thus, we have joined these degraded spectra to the SEGUE-SDSS LR spectra described in Section 2.2 for stars that were not added to the HR sample. This provided us with a total of 6451 spectra for 5001 stars (3439 RRab, 1562 RRc) that form the LR sample.

4. The New ΔS Definition

For the ΔS measurements, all HR spectra for the stars in the CHR sample were degraded to $R \approx 2000$ and rebinned with $\Delta \log(\lambda) = 0,0001$. This ensures that they are similar to the native LR spectra for which the ΔS method was developed. The equivalent widths of the lines of interest (Ca II K, H $_{\delta}$, H $_{\gamma}$, H $_{\beta}$) were measured using an updated version of the code EWIMH (Layden94; Fabrizio et al. 2019). We have adjusted the wavelength limits of the ΔS definition in order to increase sensitivity to metallicity.

Absorption lines are formed across a small range of depths in the stellar atmosphere where the thermodynamical quantities allow the transition in question to occur. Strong lines may have significant wings that were formed at different layers and trace different environments. This is especially true in nonmetallic, i.e., hydrogen, lines, often causing their very wide wings to swallow up metallic lines in their vicinity. Therefore, the fraction of the equivalent width that comes from extended wings does not necessarily represent the same thermodynamical quantities nor chemical abundance that the core of the line does.

The original Layden94 definition considered the cores but not the wings of the hydrogen lines, by using a measuring band with a width of 20 Å. For the Ca II K line, which is significantly weaker than the hydrogen lines, it employed a different measurement band depending on whether it was determined to be shallow or deep (see Figure 3 of Fabrizio et al. 2019). For the former, the band had a width of 14 Å, and for the latter, a width of 20 Å. Both wide and narrow definitions included the full line with its wings and were careful to avoid nearby lines.

The Ca II line is flanked by two strong absorption features, namely the blend of the Ca II H at 3968.5 Å with the H_{ϵ} line at 3970.0 Å, and the H_{ζ} line at 3889.1 Å. Both of them can have a dramatic effect on the continuum in very hot stars, with wings reaching as far as within ≈ 15 Å of the central wavelength of the Ca II K line. It is important to note that, as the hydrogen lines become deeper with increasing temperature, the metallic lines become shallower. Thus, it is reasonable to employ different measuring bands in each scenario. In very hot phases, however, the hydrogen lines may be so deep that the continuum

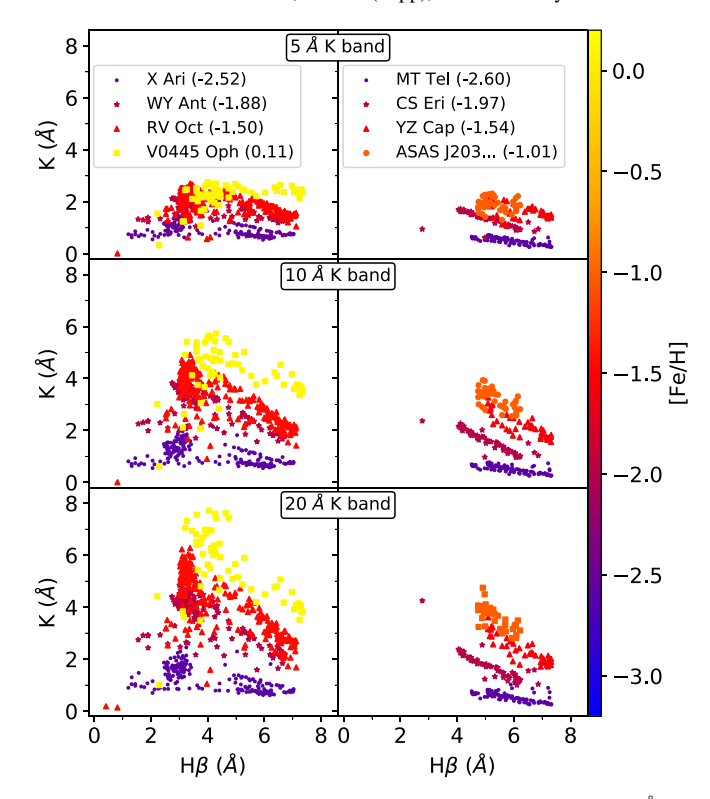


Figure 6. HK plane for H β , considering different widths (5, 10, and 20 Å) for the measurement band of the equivalent width of the Ca II K line. A group of RRab (left) and RRc (right) stars are plotted with markers colored by metallicity according to the color bar at the right edge of the figure. The considered stars are listed in the legend, with their respective high-resolution metallicities in parentheses. The name for the RRc ASAS J203145-2158.7 is shortened for convenience.

near the Ca II K line is pulled down, so to speak, by their wings. In such cases, even very narrow continuum bands will still be biased to lower values. For this reason, the original code used short continuum bands and employed a safeguard against the lowering of the continuum in hot stars: it allowed the bands to move in search of the maximum mean intensity, while keeping their length fixed. Departing from this definition, we tested combinations of the following scenarios:

- 1. Using the original wavelength range for the hydrogen lines, which includes only their cores.
- 2. Increasing the aforementioned range in order to include their wings.
- 3. Considering multiple ranges for the Ca II K line, from the innermost 2 Å of the core to the full line with its wings.
- 4. Enabling and disabling the change between "wide" and "narrow" Ca II K lines.
- 5. Changing the continuum band ranges in steps from -20% to +20%.
- 6. Enabling and disabling the movement of the continuum band for the Ca II K line.

We found that including the wings of the H lines increases scatter without any significant effect on sensitivity to metallicity. This is partly due to the presence of metallic lines in the vicinity of the H lines, as noted by Layden94. On the other hand, increasing the range of the Ca II K line to always include both core and wings with the full 20 Å width for all measurements provided the best sensitivity without significant increase in scatter (Figure 6), even for the "narrow" lines where

continuum noise may creep into the measurements. This may be due to the fact that such noise in our data is much lower than in the data used by Layden94. As the change between "narrow" and "wide" Ca II K definitions did not cause significant improvement, we have disabled it.

Furthermore, we found that the continuum band range introduces only insignificant changes. The only exception is the continuum region around the Ca II K line, due to the presence of the strong nearby absorption features. Therefore, we kept the original 15 Å range that gave enough points to define the continuum even in noisier spectra, and we saw no need to use different bandwidths on each side of the feature. We did not find a significant improvement when the continuum band was allowed to move, and so we kept its limits fixed. The final wavelength limits are shown in Figure 7 and listed in Table 6. All measurements for the CHR sample are included in Table 7.

4.1. Changes in the EWIMH Code

The EW measurements for the ΔS method can and have been done with multiple codes, among which is the IDL code EWIMH. Alongside the wavelength limits discussed in the previous section, it is crucial to establish that, in our calibration, the EW is defined as the area between the observed spectrum and the continuum, derived numerically, and not the area under a Gaussian function fit to the data.

As mentioned above, we have disabled in the EWIMH code the change between "narrow" and "wide" definitions of the Ca II K line, as well as the freedom of movement of the continuum bands around it. These two features were part of the code itself, and should be disabled in order to comply with our new empirical calibration. The other changes we made to EWIMH were done in order to make the best use of all available spectra. These changes are not essential to the calibration, although we recommend that they be added to whatever code is employed in the EW measurements.

We adapted the computation of the continuum level and equivalent widths to be more robust against emission lines caused by cosmic rays or any instrumental defect (such as dead pixels) that can mimic them. Equivalent widths are defined as the width in wavelength of a rectangle with the height of the continuum that has the same area as the area between the absorption feature and the continuum level. Generally speaking, measurement codes consider the area of emission features as negative. This means that, when a cosmic ray produces a strong enough emission feature, there is a twofold issue: (1) the real area of the line is decreased by the presence of the emission; (2) if the emission defines an area above the continuum level, this area is subtracted from the equivalent width measurement.

We have introduced a change in the code so that it will discard points with a normalized flux greater than one. This addresses the second issue by preventing negative area values, and in many cases, the first as well, because most emissions do cross the continuum level. The missing value becomes instead a simple interpolation between its closest neighbors.

The continuum level is determined by using the mean flux inside the continuum bands at each side of the line of interest. We have inserted a condition that discards normalized fluxes greater than 1.25 in these bands, thus preventing emission features or defective pixels from biasing the continuum level determination.

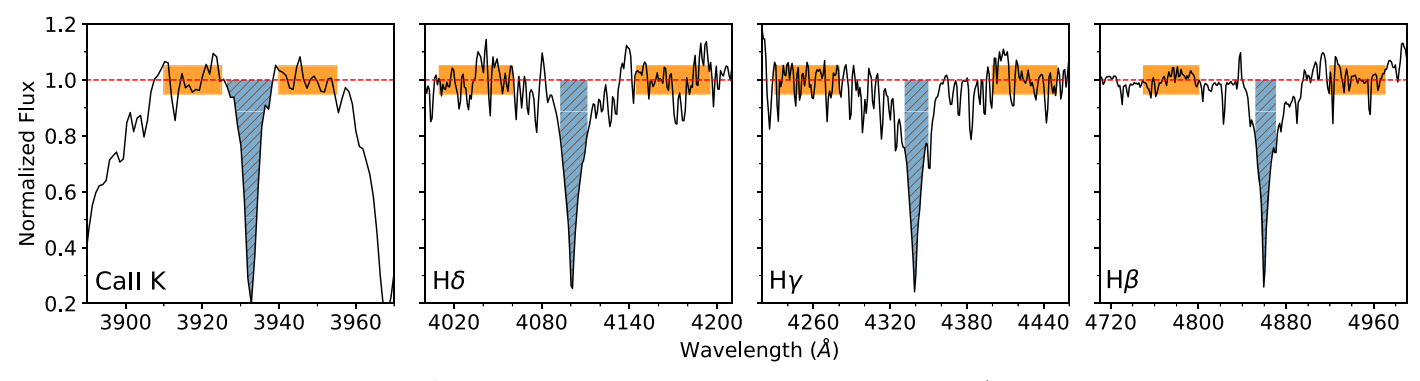


Figure 7. Wavelength ranges considered for the ΔS measurements. In black, a du Pont spectrum for AN Ser ([Fe/H] = 0.05) downgraded to a resolution R = 2000. Red dashed line indicates the continuum level. Hatched blue area denotes the area considered in the equivalent width measurement for each line. Orange shaded area indicates the region considered for the continuum level definition. Precise wavelength intervals are displayed in Table 6.

5. The New ΔS -[Fe/H] Calibration

A total of 6327 spectra for 143 stars (111 RRab, 32 RRc) were included in the CHR sample. These are the stars for which we have homogeneous HR metallicity measurements (Section 3.1). They cover a wide range in period, pulsational amplitude (Figure 2), and spectroscopic metallicity (Figure 4).

We have verified that valid equivalent widths for individual lines in individual spectra remained in the range of 0.01–10.00 Å. Values outside these limits were most often from a distorted line or continuum, and so they were discarded. To compute the ΔS index for each star, we took the median equivalent width of each feature of interest, considering all individual spectra for that star. Next, we performed a nonlinear least-squares fit using the IDL function CURVEFIT for a variety of analytical equations in the ΔS index versus spectroscopic metallicity [Fe/H] plane. The process consists of applying the equation with free coefficients to the equivalent widths of interest, deriving one ΔS value for each individual star. These values were then equaled to their respective HR [Fe/H] measurements. The code attempts to minimize the residuals by repeating this process iteratively as it changes the coefficients.

This is a significant difference between our approach and that of Layden94. Indeed, Layden94 started from the K versus H plane, where K is the equivalent width of the Ca II K line and H is the average EW of the hydrogen lines of interest. While the K versus H plane does contain a series of roughly linear sequences with slopes that are metallicity-dependent, we have verified that the ΔS index resulting from a polynomial fit done in this plane (i.e., the Layden94 equation, but with free coefficients) does not result in a tighter ΔS versus [Fe/H] relation. This is discussed in more detail in Appendix A.

Other than the original Layden94 equation, with and without free coefficients, we have also attempted a variety of functions, such as variations of it using the logarithms, polynomials, sums of Gaussians, and Moffat functions. The minimum scatter was found with a polynomial with the form

$$[Fe/H]_{\Delta S} = c_0 + c_1 K + c_2 H_{\delta} + c_3 H_{\gamma} + c_4 H_{\beta},$$
 (1)

where K, H_{δ} , H_{γ} , and H_{β} are the equivalent widths in angstroms of the Ca II K and H lines as measured in the updated EWIMH code and using the newly defined wavelength ranges (Table 6). Here, the ΔS index is already the metallicity estimate $[Fe/H]_{\Delta S}$ and no further transformations are necessary.

The quality of the fit is similar for all combinations of H lines, therefore we provide the c_n coefficients for all seven

 ${\bf Table~6} \\ {\bf Wavelength~Intervals~for~the~} \Delta S~{\bf Measurements~in~the~New~Calibration}$

Line	Interval	Start (Å)	End (Å)
Ca IIK	Left continuum	3910.00	3925.00
	Equivalent width	3923.67	3943.67
	Right continuum	3940.00	3955.00
$\overline{H_{\delta}}$	Left continuum	4010.00	4060.00
	Equivalent width	4091.74	4111.74
	Right continuum	4145.00	4195.00
$\overline{\mathrm{H}_{\gamma}}$	Left continuum	4230.00	4280.00
,	Equivalent width	4330.47	4350.47
	Right continuum	4400.00	4450.00
$\overline{\mathrm{H}_{\beta}}$	Left continuum	4750.00	4800.00
•	Equivalent width	4851.33	4871.33
	Right continuum	4920.00	4970.00

cases in Table 8. Thus, if a given spectrum has only one or two hydrogen lines, $[Fe/H]_{\Delta S}$ can still be estimated using the appropriate coefficients, with the missing H line having its corresponding c_n coefficient set to zero. The ΔS versus spectroscopic metallicity plane for all combinations is shown in Figure 8, while the corresponding values are listed in Table 9. Throughout this work, all comparisons performed against our own HR estimates or literature values were performed using the $[Fe/H]_{\Delta S}$ equation for the full set of hydrogen lines.

The behavior of the Ca II K and hydrogen lines is peculiar in phases between 0.9 and 0.1, in particular in some RRab stars with larger pulsational amplitudes (e.g., Gillet & Fokin 2014; Gillet et al. 2016). In previous calibrations of the ΔS method, these phases were neglected due to their association with the formation and propagation of shock waves, but this effect has never been investigated on a quantitative basis for the ΔS method. We have verified that the removal of this phase interval from the CHR sample results in an improvement of only 0.02 in the scatter. This is also discussed in Appendix A. Removing the RRc had similarly negligible effects.

In order to properly classify the pulsation mode of an RRL star, multiple photometric observations and possibly a light-curve template are needed so that a light curve with enough phase points can be built. Synchronizing observation time with pulsation phase requires both this detailed study and the availability of the telescope at the specific time window. If a

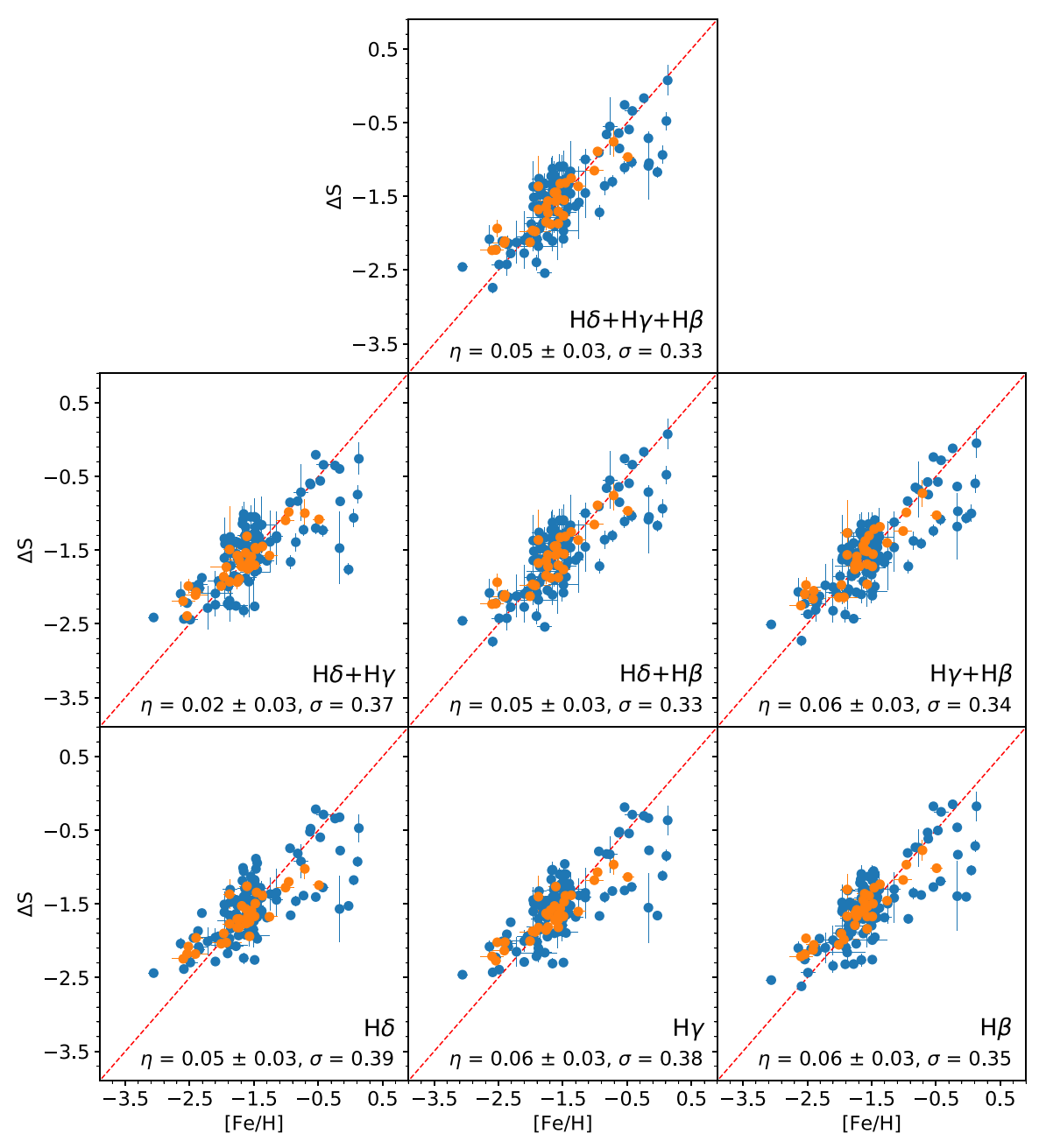


Figure 8. The ΔS vs. spectroscopic metallicity plane for all combinations of H lines, as indicated in the annotations inside each plot. Median residuals η and standard deviation of residuals σ are also indicated for each case. RRab stars are plotted in blue and RRc in orange. Dashed red lines denote the identity line.

Table 7
Individual Measurements of the Equivalent Widths of Interest for the CHR Sample

GaiaID (DR2)	HJD (day)	Ca II K (Å)	$egin{aligned} \mathbf{H}_{\delta} \ (\mathring{\mathbf{A}}) \end{aligned}$	$egin{aligned} \mathbf{H}_{\gamma} \ (\mathring{\mathbf{A}}) \end{aligned}$	$egin{array}{c} H_eta \ (m \mathring{A}) \end{array}$
15489408711727488	2455454.81452	2.14 ± 0.57	4.05 ± 0.62	4.26 ± 0.38	3.24 ± 0.35
15489408711727488	2455454.82015	1.95 ± 0.73	3.97 ± 0.46	4.34 ± 0.52	3.22 ± 0.33
15489408711727488	2455454.82434	1.94 ± 0.55	4.26 ± 0.46	4.08 ± 0.48	3.26 ± 0.54
15489408711727488	2455454.85236	1.89 ± 0.85	3.86 ± 0.48	4.18 ± 0.70	3.09 ± 0.40
15489408711727488	2455454.85655	2.09 ± 0.72	3.67 ± 0.55	3.87 ± 0.58	2.96 ± 0.41

(This table is available in its entirety in machine-readable form.)

star displays a mixed mode or any other pulsational irregularity, this synchronization may not be possible at all. This is the reason we are providing a single calibration for both

RRab and RRc at all phases. The negligible effect on the scatter when removing specific phases or separating the RRL by pulsation mode shows that previous studies of the RRLs of

H Lines	c_0	c_1	c_2	c_3	c_4	σ
$H\delta$, $H\gamma$, $H\beta$	-3.84323 ± 0.02438	0.36828 ± 0.08481	-0.22182 ± 0.11325	0.00433 ± 0.08793	0.51481 ± 0.18314	0.33
$H\delta$, $H\gamma$	-3.75381 ± 0.02682	0.39014 ± 0.09433	-0.19997 ± 0.10267	0.38916 ± 0.20318		0.37
$H\delta$, $H\beta$	-3.84160 ± 0.02302	0.36798 ± 0.05519	-0.21936 ± 0.07134	•••	0.51676 ± 0.17720	0.33
$H\gamma$, $H\beta$	-3.79074 ± 0.02462	0.35889 ± 0.07550	•••	-0.21997 ± 0.08967	0.50469 ± 0.18582	0.34
$H\delta$	-3.48130 ± 0.02690	0.36105 ± 0.02689	0.14403 ± 0.19890	•••		0.38
$H\gamma$	-3.70799 ± 0.02682	0.38127 ± 0.02831	•••	0.17973 ± 0.20453		0.38
$H\beta$	-3.92067 ± 0.02393	0.38194 ± 0.03126			0.25898 ± 0.18516	0.35

interest, in order to classify them and derive precise light curves, are unnecessary with this calibration.

Finally, the residuals do not show any clear trend with period or amplitudes, but are greater in the high-metallicity regime. This is evident in the bottom panel of Figure 9, which shows the difference between the HR [Fe/H] measurement and the LR [Fe/H] $_{\Delta S}$ estimate, plotted against the HR [Fe/H]. The larger residuals for metal-rich stars are also evident in Figure 8, where a group of about five stars deviates from the main relation, displaying lower [Fe/H] $_{\Delta S}$ values than expected. More data in the high-metallicity regime are required to further constrain the nature of the spread in ΔS values.

To constrain the accuracy of the new ΔS calibration, we estimated the metallicity distribution of the CHR sample. We found a median $\eta=-1.53\pm0.00$ and a standard deviation of $\sigma=0.49$ (Figure 9, top panel). This means that the ΔS calibration can recover the metallicity distribution based on HR estimates for the same stars. Indeed, the latter has a median [Fe/H] = -1.60 ± 0.00 and $\sigma=0.59$ (Figure 4). The median residual between both estimates is $\eta=0.05\pm0.03$, with $\sigma=0.33$.

6. Validation

To verify the accuracy of the iron abundances based on the new ΔS calibration, we performed three independent tests using iron abundances based on literature values derived from both high and LR spectra.

6.1. Comparison with HR Estimates in the Literature

Concerning the iron abundances based on HR estimates, we performed two tests. First, we took advantage of the iron abundances for field RRLs based on HR spectra available in the literature. These have already been discussed during the validation of our HR metallicities (Section 4), and the shifts (Δ) to move them in the current metallicity scale are listed in Table 5. They are included in the HR sample and contain 64 objects in common with the CHR sample. We found that the median difference between the new [Fe/H] $_{\Delta S}$ and the literature HR estimates rescaled into our scale is $\eta = 0.12 \pm 0.04$, $\sigma = 0.36$ (Figure 10, top panel).

Second, we computed ΔS metallicities for 12 RRLs that belong to Galactic GCs. The GC metallicities were provided by Carretta et al. (2009) in a new scale they constructed from HR estimates. No scale transformation was performed. The residuals of the comparison resulted in a median $\eta = -0.08 \pm 0.04$ and $\sigma = 0.16$ (Figure 10, bottom panel).

6.2. Comparison with LR Estimates in the Literature

The RRab in the SEGUE-SDSS data set were investigated in detail by F19 using the Layden94 definition. Considering the 2385

RRab in common between both works, their estimates produce a metallicity distribution with median $[\text{Fe/H}]_{F19} = -1.60 \pm 0.01$ and $\sigma = 0.40$. Meanwhile, the new definition applied to the same stars provides $[\text{Fe/H}]_{\Delta S} = -1.48 \pm 0.01$ and $\sigma = 0.39$. The top panel of Figure 11 shows the residuals of this comparison.

Liu et al. (2020) constructed a large catalog of Galactic RRL with metallicities estimated from LR spectral matching. They made use of spectra from both SEGUE-SDSS and the LAMOST Experiment for Galactic Understanding and Exploration (Zhao et al. 2012). A total of 2634 of their stars are included in our SEGUE-SDSS sample, allowing us to make a direct comparison between the two different approaches to metallicity estimation. Interestingly, their spectral matching technique relies on using precisely the Ca II K line and the same three Balmer lines of the ΔS method. The median difference between their values and the ones derived in this work is $\eta = -0.23 \pm 0.00$ with $\sigma = 0.24$ (Figure 11, middle panel). The residuals are very similar for both the RRc $(\eta = -0.21 \pm 0.01, \sigma = 0.23)$ and the RRab $(\eta = -0.23 \pm 0.01, \ \sigma = 0.24)$. Note that the HR estimates they adopted to validate their method are, for 18 out of 19 stars, from Pancino et al. (2015) and Nemec et al. (2013). These two works are included in our HR comparison and also present a similar shift (Figure 5 and Table 5). Therefore, this scale difference of ≈ -0.2 between their results and ours is to be expected.

Finally, no validation would be complete without considering Dambis (2009) (D09), a compilation of RRL metallicities widely used in the literature. In order to keep the metallicity scale as homogeneous as possible, D09 adopted the values from Layden94 and Layden et al. (1996) wherever they were available, complementing them with other sources after these were transformed into the same Layden94 scale, which is the Zinn & West (1984) scale. In our comparison of 102 stars in common between their work and the new [Fe/H] $_{\Delta S}$ estimates for both the calibrating and LR samples, we found a shift of $\eta=0.16\pm0.03$, $\sigma=0.30$. However, to avoid having metallicities transformed into one scale and then transformed once more into another scale, we will provide the corrections for the different D09 sources separately in a forthcoming paper.

6.3. Comparison with Other LR Spectrographs

We investigated the accuracy of the new $[Fe/H]_{\Delta S}$ calibration in estimating the metallicity of individual RRLs when applied to native LR spectra collected with different instrument and telescope combinations. In particular, we have secured a set of LAMOST DR6 spectra for RRLs in common either with the LR sample or with the HR sample. The new calibration was only applied to LAMOST spectra with S/N larger than 10 in the region of the Ca II K line. Afterward, we visually inspected all the spectra with S/N between 10 and 20

Crestani et

GaiaID (DR2)	Class	$N_{ m spec}$	$[H\delta, H\gamma, H\beta]$ (dex)	$[H\delta, H\gamma]$ (dex)	$[H\delta, H\beta]$ (dex)	$[H\gamma, H\beta]$ (dex)	[Hδ] (dex)	$[H\gamma]$ (dex)	[Hβ] (dex)
15489408711727488	RRab	194	-2.74 ± 0.07	-2.43 ± 0.05	-2.74 ± 0.07	-2.73 ± 0.07	-2.38 ± 0.02	-2.43 ± 0.02	-2.62 ± 0.03
77849374617106176	RRab	6	-1.62 ± 0.15	-1.56 ± 0.14	-1.61 ± 0.15	-1.56 ± 0.15	-1.44 ± 0.07	-1.51 ± 0.08	-1.56 ± 0.08
80556926295542528	RRc	3	-1.36 ± 0.41	-1.49 ± 0.58	-1.36 ± 0.41	-1.27 ± 0.45	-1.37 ± 0.20	-1.40 ± 0.28	-1.30 ± 0.21
630421935431871232	RRab	3	-1.85 ± 0.51	-1.93 ± 0.48	-1.85 ± 0.51	-1.80 ± 0.47	-1.84 ± 0.23	-1.88 ± 0.23	-1.84 ± 0.25
1167409941124817664	RRc	1	-1.68 ± 0.00	-1.93 ± 0.00	-1.68 ± 0.00	-1.56 ± 0.00	-1.77 ± 0.00	-1.82 ± 0.00	-1.67 ± 0.00

Note. Columns 4–10 indicate between square brackets the combinations of hydrogen lines considered in the measurement.

(This table is available in its entirety in machine-readable form.)

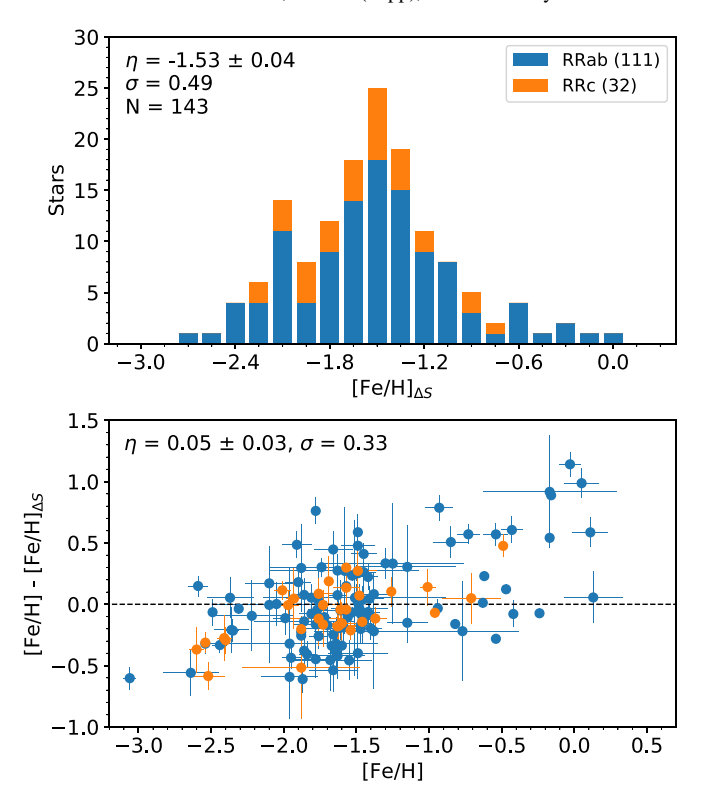


Figure 9. Top: $[Fe/H]_{\Delta S}$ distribution for the CHR sample. For reference, the distribution of high-resolution measurements for the same sample is shown in the top panel of Figure 4. Bottom: residuals of the new ΔS calibration vs. spectroscopic metallicity. RRab are plotted in blue, and RRc in orange.

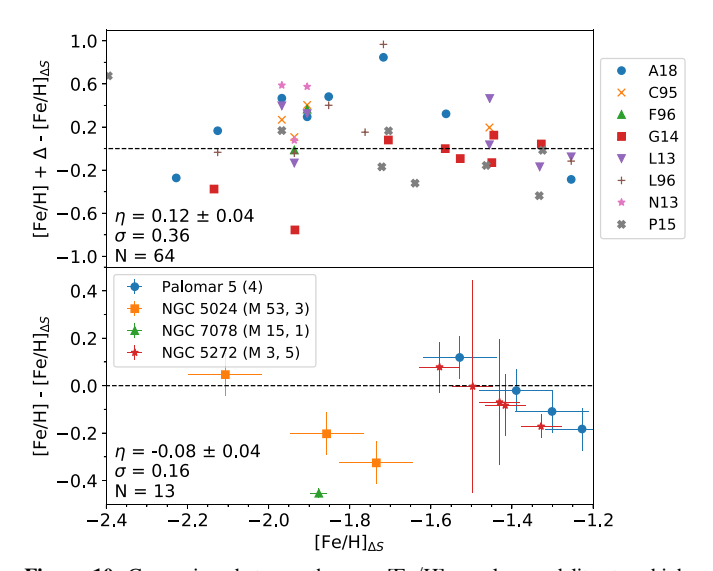


Figure 10. Comparison between the new $[Fe/H]_{\Delta S}$ values and literature high-resolution metallicities for RRL stars. Top: field RRL with literature values brought to our scale by the addition of the corresponding shift (Δ) . References and shifts are listed in Table 5. Bottom: globular cluster RRL considering the cluster metallicities derived by Carretta et al. (2009), which provides their value on a scale based on high-resolution spectra. No shift has been applied to these values.

for a supplementary quality check before including them in the current analysis.

This resulted in a LAMOST sample of 569 LR spectra for 364 RRLs (203 RRab, 161 RRc). For 321 of these RRLs, we have $[Fe/H]_{\Delta S}$ estimates coming from the LR sample, while for 43 of them, we have [Fe/H] measurements in the HR sample. The $[Fe/H]_{\Delta S}$ values derived from LAMOST spectra using the three

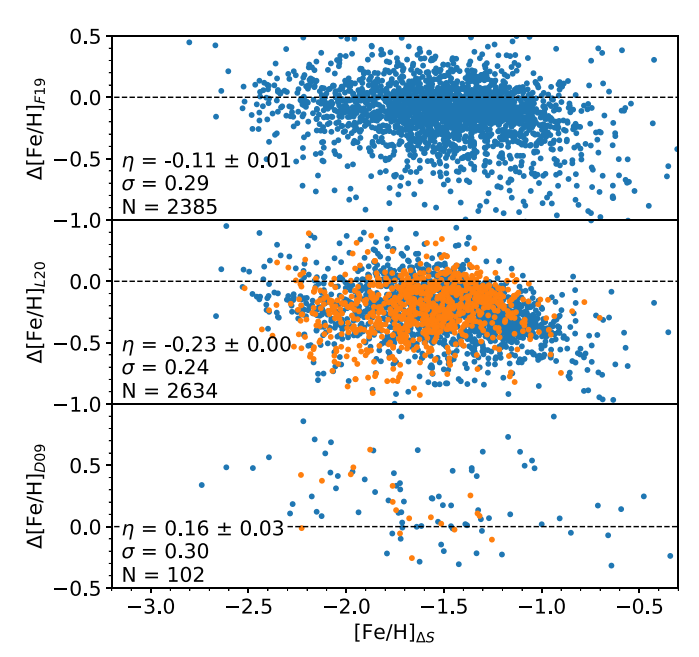


Figure 11. Difference $\Delta[\text{Fe/H}]$ – $[\text{Fe/H}]_{\Delta S}$ between the new $[\text{Fe/H}]_{\Delta S}$ values and those derived by Fabrizio et al. (2019) with the SEGUE-SDSS data set using the Layden94 definition ($\Delta[\text{Fe/H}]_{F19}$, top panel), Liu et al. (2020) with the SEGUE-SDSS and LAMOST data sets but using low-resolution spectral matching ($\Delta[\text{Fe/H}]_{L20}$, middle panel), and the Dambis (2009) compilation ($\Delta[\text{Fe/H}]_{L00}$, bottom). RRab are plotted in blue, and RRc in orange.

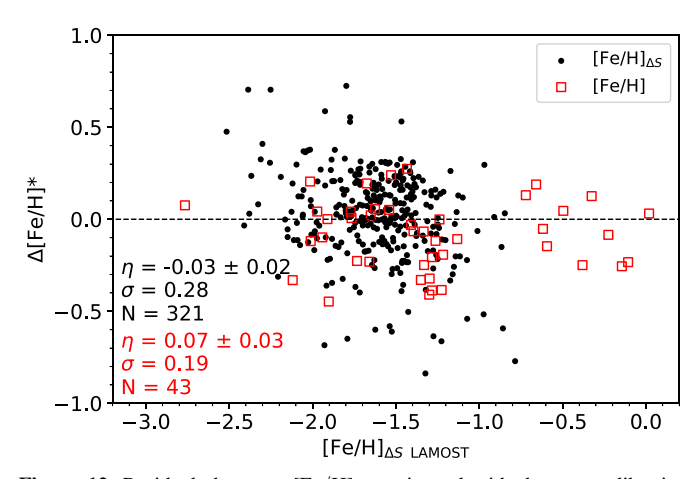


Figure 12. Residuals between $[Fe/H]_{\Delta S}$ estimated with the new calibration applied to the RRLs of the LAMOST data set, and the corresponding metallicities of the LR (black dots) and the HR (red squares) samples. The medians η , standard deviations σ , and sample sizes N are shown in black for the LR results, and in red for the HR results.

hydrogen lines show no trend when compared to iron abundances based on the HR measurements (Figure 12). The same outcome applies to the comparison with the LR sample. Indeed, the residuals show a larger scatter ($\sigma = 0.28$ dex versus $\sigma = 0.19$ dex), but they are within the typical uncertainties of the method.

These good correlations indicate that the new $[Fe/H]_{\Delta S}$ calibration, when applied to LR spectra collected with different spectrographs, provides metal abundances that are on the same scale. The same outcome applies to the comparison with the LR sample. Indeed, the residuals show a larger scatter ($\sigma = 0.28$ dex versus $\sigma = 0.19$ dex), but they are within the typical uncertainties of the method.

In passing, we also note that the SEGUE-SDSS and the LAMOST data sets, when considered together, include 11

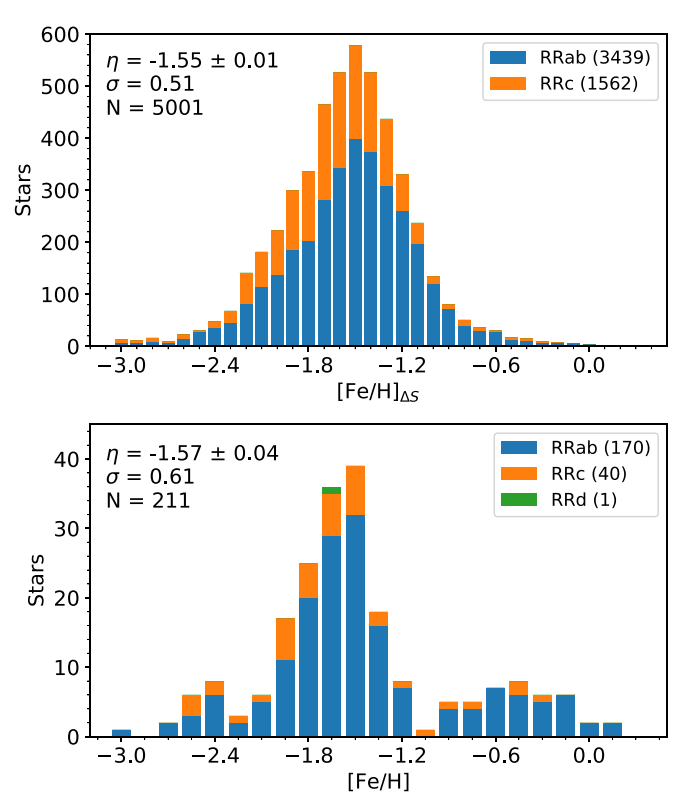


Figure 13. Top: distribution of metallicities based on the new ΔS definition for LR sample, consisting of 5001 Galactic halo RRL stars (3439 RRab, 1562 RRc). Bottom: HR sample, consisting of 211 RRL (170 RRab, 40 RRc, 1 RRd) from this work and the literature, with the latter brought into our scale. RRab, RRc, and RRd are plotted, respectively, in blue, orange, and green.

RRLs with a number of randomly collected spectra ranging from 5 to 15. To further investigate possible variations in metal abundances along the pulsation cycle, we applied the new calibration to these LR spectra collected with different spectrographs. We found a median standard deviation per RRL of \sim 0.15 dex, in very good agreement with results based on the degraded HR spectra (see Table 9).

7. Application of the New ΔS Calibration

7.1. Metallicity Distribution of Field RRL

Our new empirical $[Fe/H]_{\Delta S}$ calibration allowed us, for the first time in the literature, to probe the metallicity distribution of the Galactic halo by applying the ΔS method to both RRab and RRc stars. Toward this end, we employed the LR sample. It contains no stars in common with the HR sample, which we will analyze separately.

The resulting $[{\rm Fe/H}]_{\Delta S}$ distribution has a median $\eta=-1.55\pm0.01$ and $\sigma=0.51$ (Figure 13, top panel). The RRc display generally lower metallicities. Separating fundamental and first-overtone pulsators results in medians that differ by 0.12, with the RRab peaking at $[{\rm Fe/H}]_{\Delta S}=-1.51\pm0.01$, with $\sigma=0.50$. Meanwhile, the values for the RRc are $[{\rm Fe/H}]_{\Delta S}=-1.63\pm0.01$ and $\sigma=0.50$.

The lower metallicity distribution for the RRc is also found in the results of Liu et al. (2020). Considering the stars in common between their work and ours, but their metallicity results, the RRab present $\eta = -1.69 \pm 0.01$, $\sigma = 0.35$, while for the RRc, the values are $\eta = -1.80 \pm 0.01$, $\sigma = 0.38$. As mentioned in the previous section, there is a zero-point shift of

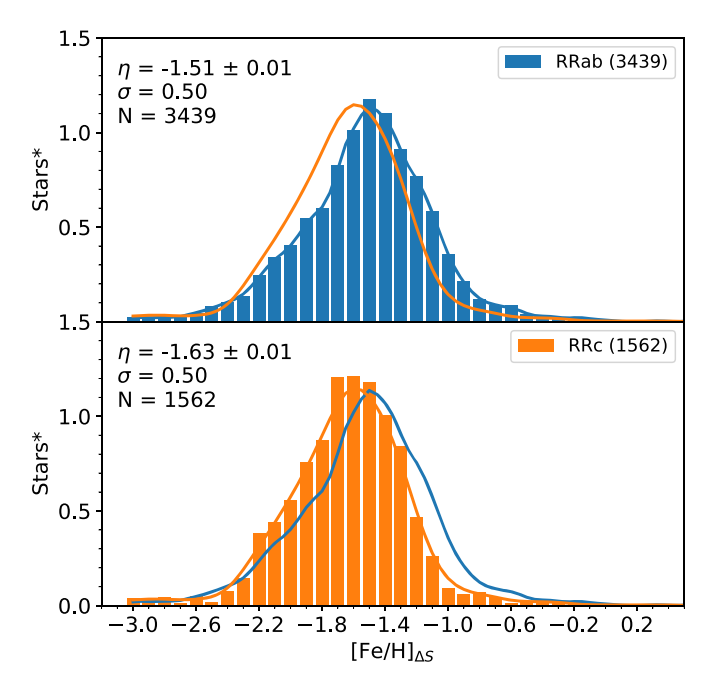


Figure 14. Area-normalized histograms of $[Fe/H]_{\Delta S}$ for the LR sample. RRab are plotted in blue in the top panel, and RRc in orange in the bottom panel. Full lines represent the Gaussian-smoothed distributions for the RRab and the RRc, in blue and orange, respectively. They are shown together on both panels for comparison.

about 0.2 between their scale and ours that begins with the HR reference scale each work adopted.

Interestingly, the metallicity distribution as a whole is asymmetrical and cannot be adequately described by a single Gaussian, as is also the case for the kinematic distribution of the field halo stars (e.g., Lancaster et al. 2019). The slope in the metalrich regime is steeper than in its metal-poor counterpart. In this context, it is worth mentioning that the difference between the metallicity distribution of RRab and RRc is further supported by their asymmetry (skewness). Figure 14 shows that the metal-rich tail of both RRab and RRc agrees quite well in the metal-rich regime. However, in the metal-poor regime, the RRc display a broader peak and steeper slope ([Fe/H] $_{\Delta S} \lesssim -1.8$). This evidence indicates that the production rate of first-overtone variables decreases as the metallicity of the stellar environment increases. This trend is expected because the metallicity is the most relevant parameter in shaping the morphology of the horizontal branch (Torelli et al. 2019) and in turn the sampling of the RRL instability strip (Bono et al. 1997, 2011).

7.2. The New ΔS Calibration Applied to a Mixed-mode Variable

We also note that we have applied the new calibration to a field mixed-mode variable (ASAS J183952-3200.9). On the basis of ten HR spectra collected with X-Shooter and two with FEROS, we estimated an iron abundance of $[Fe/H] = -1.62 \pm 0.10$. All 12 estimates were made from individual spectra, i.e., without stacking. The $[Fe/H]_{\Delta S}$ abundance, based on the new ΔS calibration applied to the same spectra but degraded to a spectral resolution of R = 2000, agrees quite well with $[Fe/H]_{\Delta S} = -1.51 \pm 0.12$. This is the first time that the metallicity of an RRd is estimated by using ΔS , and the remarkable agreement with the direct measurement further supports the plausibility of a single ΔS calibration for all RRLs regardless of their pulsation mode.

8. Summary and Final Remarks

We have provided a new calibration of the ΔS method to derive LR spectroscopic metallicity estimates for RRL stars. It departs directly from the ΔS versus [Fe/H] plane and makes use of homogeneous HR metallicity measurements for 143 RRLs (111 RRab, 32 RRc) from a variety of spectrographs. The calibrating stars display a wide range of pulsational amplitudes and periods. They cover over three dex in iron abundance, including the metalpoor and metal-rich tails that were poorly sampled in previous works. The most metal-poor star in the CHR sample, with two HR measurements resulting in [Fe/H] = -3.06 ± 0.08 , may be among the most metal-poor RRLs ever identified (Wallerstein et al. 2009; Hansen et al. 2011). The metal-rich tail is similarly remarkable, with multiple stars presenting supersolar metallicities and pointing to a complex chemical enrichment history.

For the first time, this empirical calibration includes the full pulsation cycle as well as first-overtone pulsators. Therefore, it is not necessary to classify the pulsation mode of the RRL of interest, nor to execute timed observations in order to gather the data at specific phase intervals. This means no detailed knowledge of the light curve is required.

While we suggest preference be given to the calibration with all Balmer lines $(H_{\delta}, H_{\gamma}, H_{\beta})$ when possible, followed by combinations that include H_{β} , we also provide coefficients for all combinations of one or two of these lines. We have employed both SEGUE-SDSS ($R \approx 2000$) and LAMOST ($R \approx 1500$) spectra in order to investigate whether the new calibration is valid for LR spectra collected with different spectrographs. Our findings support that the new calibration can be applied to different spectrographs and resolutions. This means that there is no need for transformations between different equivalent width systems in order to obtain metallicity estimates within the typical uncertainties of the method. We also provide 211 reference stars covering a wide range in metallicity in HR, 144 of which have also $[Fe/H]_{\Delta S}$ estimates based on all combinations of Balmer lines. This is the largest sample of HR measurements for field RRL stars in the literature, and can be used to anchor any future works in our metallicity scale.

We have applied the new ΔS calibration to a sample of 5001 field RRLs (3439 RRab, 1562 RRc) with either SEGUE-SDSS LR spectra or HR spectra downgraded and rebinned in order to mimic the SEGUE-SDSS spectra. This resulted in a distribution with median $\eta = -1.55 \pm 0.01$ and $\sigma = 0.51$, in good agreement with previous studies of halo RRLs. For comparison, the HR sample described above has a distribution with $\eta = -1.57 \pm 0.04$ and $\sigma = 0.61$. In both cases, the distribution for the RRc alone peaks at slightly lower metallicities than the RRab. Furthermore, the metallicity distributions of the RRab and RRc, when considered separately, have different profiles in the metal-poor regime. Indeed, the slope of the distribution is shallower for the RRc. This difference in the profiles and the ≈0.1 difference in the peaks of the two distributions support the theoretical scenario of a steady decrease in the production of RRc as the metallicity of the stellar environment increases.

It is a real pleasure to thank the anonymous referee for positive remarks concerning the content and the results of this investigation, as well as for pertinent suggestions that improved the readability of the paper.

This research has made use of the National Aeronautics and Space Administration (NASA) Astrophysics Data System, the National Institute of Standards and Technology (NIST) Atomic

Spectra Database, the JVO Portal²⁹ operated by ADC/NAOJ, and the ESO Science Archive Facility.

Based on observations made with the Italian Telescopio Nazionale Galileo (TNG) operated on the island of La Palma by the Fundación Galileo Galilei of the INAF (Istituto Nazionale di Astrofisica) at the Spanish Observatorio del Roque de los Muchachos of the Instituto de Astrofisica de Canarias.

Some of the observations reported in this paper were obtained with the Southern African Large Telescope (SALT).

Based on observations collected at the European Organisation for Astronomical Research in the Southern Hemisphere under ESO programmes 0100.D-0339, 0101.D-0697, 0102.D-0281, 076.B-0055, 077.B-0359, 077.D-0633, 079.A-9015, 079.D-0262, 079.D-0462, 079.D-0567, 082.C-0617, 083.B-0281, 083. C-0244, 094.B-0409, 095.B-0744, 097.A-9032, 098.D-0230, 189. B-0925, 267.C-5719, 297.D-5047, 67.D-0321, 67.D-0554, 69.C-0423, 71.C-0097, 0100.D-0273, 083.C-0244, 098.D-0230.

Guoshoujing Telescope (the Large Sky Area Multi-Object Fiber Spectroscopic Telescope, LAMOST) is a National Major Scientific Project built by the Chinese Academy of Sciences. Funding for the project has been provided by the National Development and Reform Commission. LAMOST is operated and managed by the National Astronomical Observatories, Chinese Academy of Sciences.

Funding for the SDSS and SDSS-II has been provided by the Alfred P. Sloan Foundation, the Participating Institutions, the National Science Foundation, the U.S. Department of Energy, the National Aeronautics and Space Administration, the Japanese Monbukagakusho, the Max Planck Society, and the Higher Education Funding Council for England. The SDSS Web Site is http://www.sdss.org/. The SDSS is managed by the Astrophysical Research Consortium for the Participating Institutions. The Participating Institutions are the American Museum of Natural History, Astrophysical Institute Potsdam, University of Basel, University of Cambridge, Case Western Reserve University, University of Chicago, Drexel University, Fermilab, the Institute for Advanced Study, the Japan Participation Group, Johns Hopkins University, the Joint Institute for Nuclear Astrophysics, the Kavli Institute for Particle Astrophysics and Cosmology, the Korean Scientist Group, the Chinese Academy of Sciences (LAMOST), Los Alamos National Laboratory, the Max-Planck-Institute for Astronomy (MPIA), the Max-Planck-Institute for Astrophysics (MPA), New Mexico State University, Ohio State University, University of Pittsburgh, University of Portsmouth, Princeton University, the United States Naval Observatory, and the University of Washington.

We acknowledge financial support from US NSF under Grants AST-1714534 (M. M., J. P. M.) and AST1616040 (CS). E. K. G., B. L., Z. D., and H. L. were supported by the Deutsche Forschungsgemeinschaft (DFG, German Research Foundation) Project-ID 138713538—SFB 881 ("The Milky Way System," subprojects A03, A05, A11). E. V. acknowledges the Excellence Cluster ORIGINS Funded by the DFG under Germany's Excellence Strategy- EXC-2094-390783311.

Appendix Equivalent Width Dependence on Metallicity and Phase

This work departed directly from the ΔS versus spectroscopic metallicity plane in order to find the best analytical equation and parameters relating these two quantities. The

15

http://jvo.nao.ac.jp/portal/

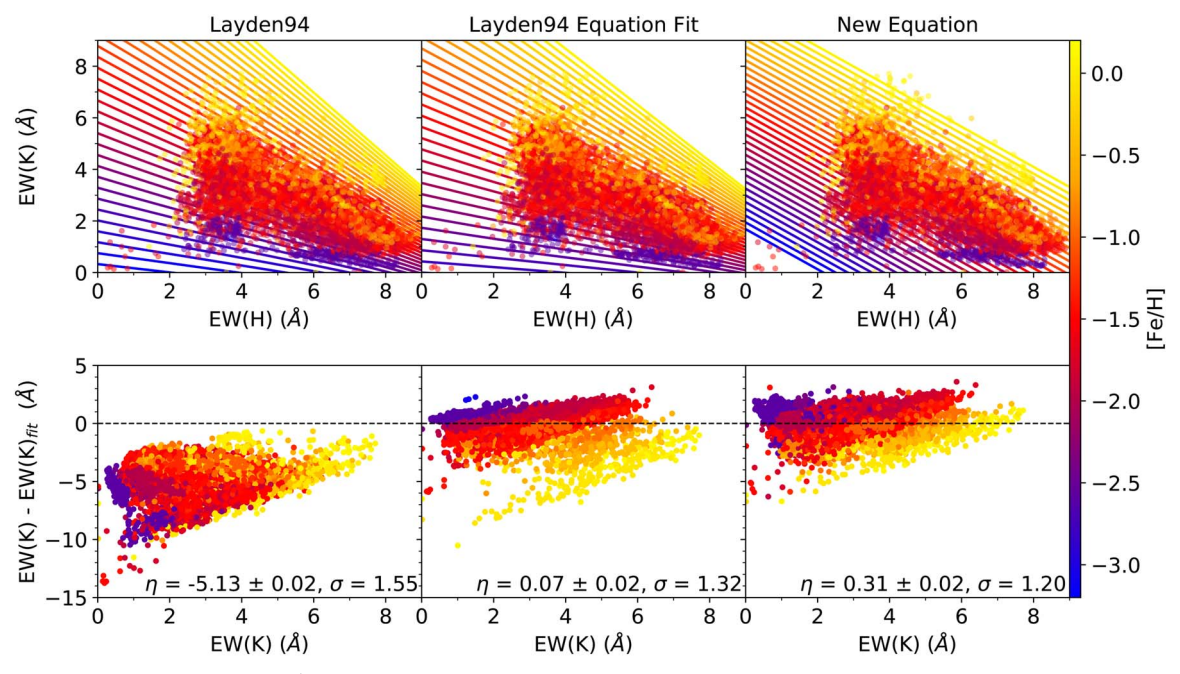


Figure 15. HK plane (top) and residuals of the ΔS (bottom) for the CHR sample considering three cases: the original Layden94 equation (left), a fit of the Layden94 equation with new coefficients (middle), and the new equation (right). Points are the measured EW values in the new definition of wavelength ranges. Lines in the top panels are the predicted Ca II K equivalent width considering each equation for a range of metallicity values. Data points and analytical lines are colored by high-resolution metallicity according to the color bar at the right edge of the figure.

original Layden94 equation, however, departed from a polynomial fit in the HK plane, resulting in a relation with the form

$$K = a + bH + c[Fe/H] + dH[Fe/H], \tag{A1}$$

where a to d are constants, K the EW of the Ca II K line, and H the mean EW for the three H lines. This is a very reasonable strategy, as there is a clear pattern for the RRL in this plane, with stars of similar metallicity clustering in a somewhat linear fashion, with a slope and intercept that increases with metallicity (Figure 15). Thus, we attempted a new fit of the coefficients of this equation. The result created a larger overall scatter in the ΔS -[Fe/H] plane, with σ_r greater by 0.12. Furthermore, it could not trace the metal-rich regime. The polynomial equation derived in this work, on the other hand, does not contain a metallicity-dependent slope in the HK plane. This, in turn, yielded a tighter relation that can reach the metalrich regime (Figure 6). A comparison in the ΔS -[Fe/H] plane between the polynomial fit adopted in this work and the Layden94 equation with new coefficients is shown in Figure 16.

The original Layden94 definition did not include rising branch phases due to the shock waves that occur at this point of the pulsation cycle and can distort the profile of the Balmer lines. This phase avoidance introduces the burdensome necessity of properly phasing the RRL and timing observations in such a way as to avoid these phases. Adequate light curves and reference epochs require multiple previous observations that may not be readily available. Furthermore, as discussed previously, the duration of the line-distorting shock waves is very brief.

In the HK plane, stars in these phases occupy a region underneath the area created by the other phases, effectively creating a "loop" that invades a lower-metallicity region. Figure 17 illustrates the origin of the "loops." Their lower sequence is caused by not only a sharp peak in the EW of the H lines but also a sudden dip in the EW of the Ca II K line. Both the H and the Ca II K lines are strongly responsive to the effective temperature, albeit in opposite directions, i.e., the EW of H lines increases with temperature, while that of the Ca II K decreases. Therefore, deriving metallicities from a combination of these lines relies on this mirrored effect that nullifies the influence of the temperature on the equivalent width of the Ca II K, effectively isolating the metallicity impact. However, the peak of the H lines and the dip of the Ca II K lines in EW are not perfectly synchronized, with the latter occurring slightly earlier. Thus, at phase 0.9–0.1, we observe a sudden drop of any value that relates these two quantities, as evident in the bottom panels of Figure 18.

Note that the EW variation of the lines of interest in the RRc is significantly smoother. This is also true for their light curves, which are almost sinusoidal while those of their fundamental mode counterparts are sawtooth-shaped. The Ca II K line dip is not identical among RRab stars either. There is some evidence that more metal-rich stars will display a deeper dip, but other characteristics such as pulsational amplitude may play a role.

In order to investigate the effect of phases between 0.9 and 0.1 in the final ΔS value, we have removed them from the sample and performed a new fit of the coefficients of the polynomial equation and of the Layden94 equation. We found that this produced slightly smaller median residuals and slightly larger scatter for the new equation (Figure 16). For the Layden94 equation, the phase cut caused both quantities to increase over 0.2. This phase interval, therefore, has only a minimal effect on the ΔS computation with the new equation.

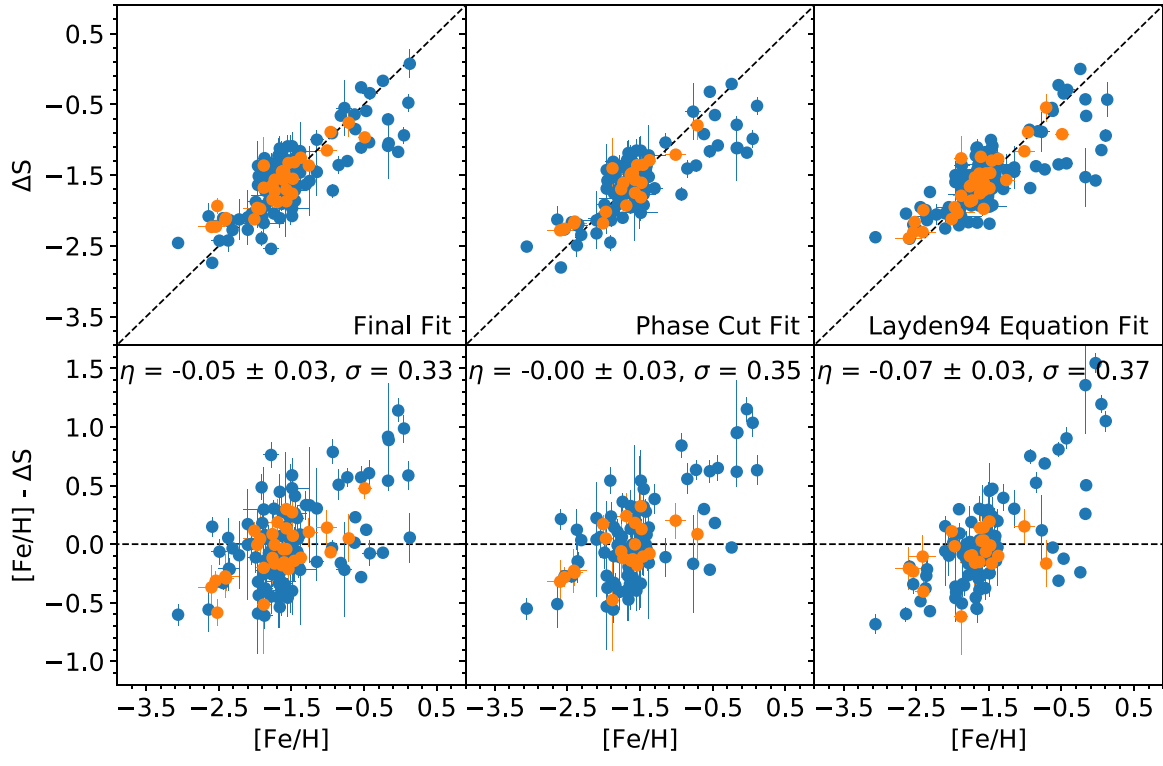


Figure 16. The ΔS -[Fe/H] plane (top) and residuals (bottom) for three cases considering all H lines: the final polynomial fit adopted in this work (left), the polynomial fit derived from the sample with phases between 0.1 and 0.9 (middle), and the fit of the Layden94 equation with new coefficients (right). RRab are plotted in blue, and RRc in orange.

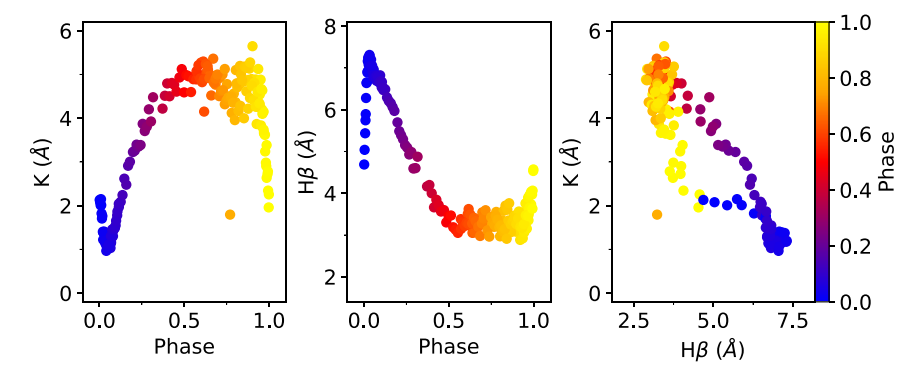


Figure 17. Equivalent widths for the Ca II K (left) and H β (middle) lines, and the HK plane (right) for HH Pup. Symbols are colored according to phase.

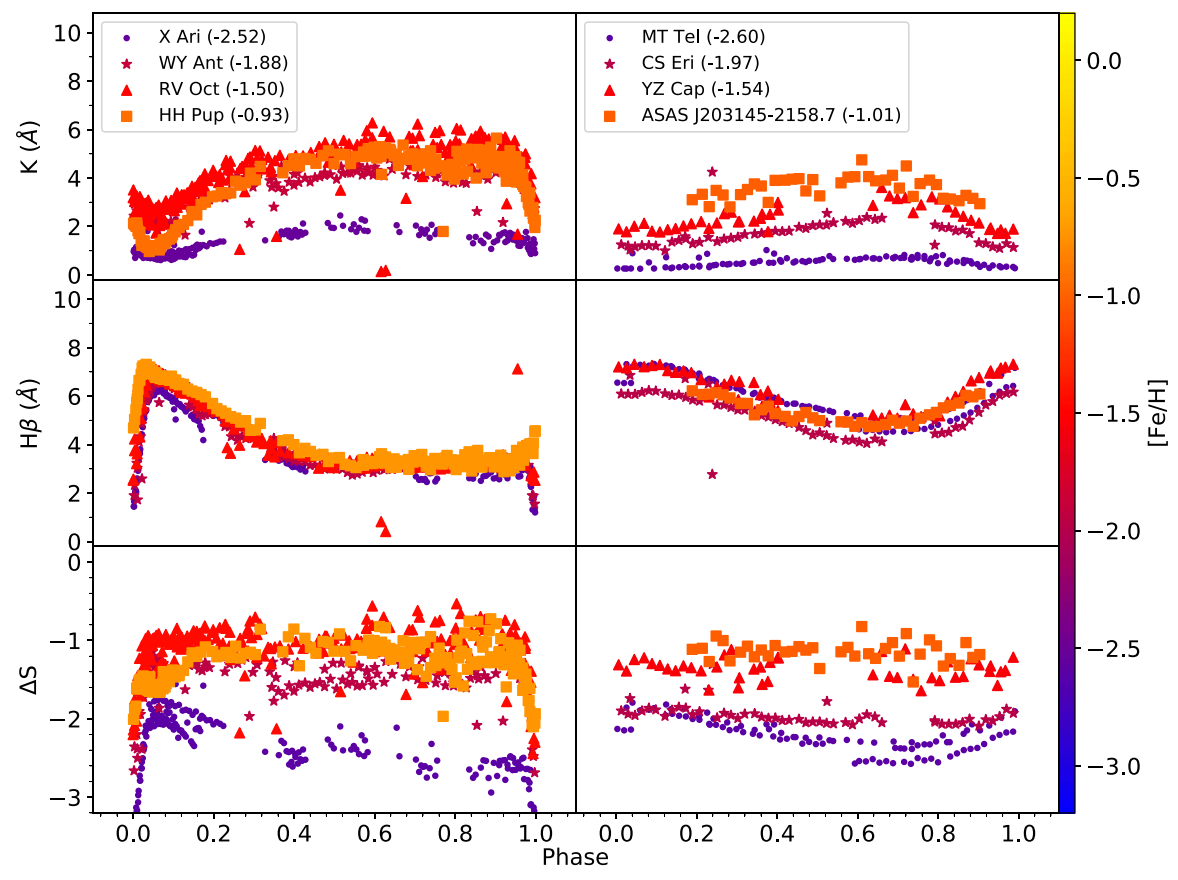


Figure 18. Behavior of the equivalent width of the Ca II K line (top), H β line (middle), and ΔS value (bottom) across the entire pulsation cycle for three RRab (left panels) and three RRc (right panels). Points are colored by metallicity according to the color bar on the right edge of the figure. The considered stars are listed in the legend, with their respective high-resolution metallicities between parentheses.

ORCID iDs

J. Crestani https://orcid.org/0000-0001-8926-3496 M. Fabrizio https://orcid.org/0000-0001-5829-111X V. F. Braga https://orcid.org/0000-0001-7511-2830 C. Sneden https://orcid.org/0000-0002-3456-5929 G. Bono https://orcid.org/0000-0002-4896-8841 V. D'Orazi https://orcid.org/0000-0002-2662-3762 M. Monelli https://orcid.org/0000-0001-5292-6380 J. Storm https://orcid.org/0000-0002-8627-6096 B. Chaboyer https://orcid.org/0000-0003-3096-4161 M. Dall'Ora https://orcid.org/0000-0001-8209-0449 G. Fiorentino https://orcid.org/0000-0003-0376-6928 E. K. Grebel https://orcid.org/0000-0002-1891-3794 M. Marengo https://orcid.org/0000-0001-9910-9230 C. E. Martínez-Vázquez https://orcid.org/0000-0002-9144-7726 J. P. Mullen https://orcid.org/0000-0002-1650-2764 J. Neeley https://orcid.org/0000-0002-8894-836X P. B. Stetson https://orcid.org/0000-0001-6074-6830 F. Thévenin https://orcid.org/0000-0002-5032-2476 E. Valenti https://orcid.org/0000-0002-6092-7145

References

Andrievsky, S., Wallerstein, G., Korotin, S., et al. 2018, PASP, 130, 024201 Asplund, M., Grevesse, N., Sauval, A. J., & Scott, P. 2009, ARA&A, 47, 481 Bard, A., Kock, A., & Kock, M. 1991, A&A, 248, 315 Bard, A., & Kock, M. 1994, A&A, 282, 1014 Belmonte, M. T., Pickering, J. C., Ruffoni, M. P., et al. 2017, ApJ, 848, 125

Blackwell, D. E., Booth, A. J., Haddock, D. J., Petford, A. D., & Leggett, S. K. 1986, MNRAS, 220, 549 Blackwell, D. E., Petford, A. D., & Shallis, M. J. 1979, MNRAS, 186, 657 Blackwell, D. E., Petford, A. D., Shallis, M. J., & Simmons, G. J. 1982, MNRAS, 199, 43 Bono, G., Braga, V. F., Crestani, J., et al. 2020a, ApJL, 896, L15 Bono, G., Braga, V. F., Fiorentino, G., et al. 2020b, A&A, 644, A96 Bono, G., Caputo, F., Castellani, V., et al. 2003, MNRAS, 344, 1097 Bono, G., Caputo, F., Castellani, V., & Marconi, M. 1997, A&AS, 121, 327 Bono, G., Dall'Ora, M., Caputo, F., et al. 2011, in Astrophysics Ser. 5, RR Lyrae Stars, Metal-Poor Stars, and the Galaxy, Carnegie Observatories, ed. A. McWilliam (Pasadena, CA: The Observatories of the Carnegie Institution of Washington), 1 Bono, G., Iannicola, G., Braga, V. F., et al. 2019, ApJ, 870, 115 Bono, G., & Stellingwerf, R. F. 1992, MmSAI, 63, 357 Braga, V. F., Stetson, P. B., Bono, G., et al. 2016, AJ, 152, 170 Braga, V. F., Stetson, P. B., Bono, G., et al. 2018, AJ, 155, 137 Bridges, J. M., & Kornblith, R. L. 1974, ApJ, 192, 793 Butler, D. 1975, ApJ, 200, 68 Butler, D., Carbon, D., & Kraft, R. P. 1976, ApJ, 210, 120 Butler, D., Kinman, T. D., & Kraft, R. P. 1979, AJ, 84, 993 Carretta, E., Bragaglia, A., Gratton, R., D'Orazi, V., & Lucatello, S. 2009, &A, 508, 695 Castelli, F., & Kurucz, R. L. 2003, in IAU Symp. 210, Modelling of Stellar Atmospheres, ed. N. Piskunov, W. W. Weiss, & D. F. Gray (San Francisco, CA: ASP), A20 Chadid, M., Sneden, C., & Preston, G. W. 2017, ApJ, 835, 187 Chadid, M., Vernin, J., & Gillet, D. 2008, A&A, 491, 537 Clementini, G., Carretta, E., Gratton, R., et al. 1995, AJ, 110, 2319 Crause, L. A., Sharples, R. M., Bramall, D. G., et al. 2014, Proc. SPIE, 9147, 91476T

Cropper, M., Katz, D., Sartoretti, P., et al. 2018, A&A, 616, A5

Dambis, A. K., Berdnikov, L. N., Kniazev, A. Y., et al. 2013, MNRAS,

Dambis, A. K. 2009, MNRAS, 396, 553

435, 3206

```
Den Hartog, E. A., Lawler, J. E., Sneden, C., Cowan, J. J., & Brukhovesky, A.
  2019, ApJS, 243, 33
Den Hartog, E. A., Ruffoni, M. P., Lawler, J. E., et al. 2014, ApJS, 215, 23
Drake, A. J., Catelan, M., Djorgovski, S. G., et al. 2013a, ApJ, 763, 32
Drake, A. J., Catelan, M., Djorgovski, S. G., et al. 2013b, ApJ, 765, 154
Drake, A. J., Djorgovski, S. G., Catelan, M., et al. 2017, MNRAS, 469, 3688
Evans, D. W., Riello, M., De Angeli, F., et al. 2018, A&A, 616, A4
Fabrizio, M., Bono, G., Braga, V. F., et al. 2019, ApJ, 882, 169
Fernley, J., & Barnes, T. G. 1996, A&A, 312, 957
For, B.-Q., Sneden, C., & Preston, G. W. 2011, ApJS, 197, 29
Freeman, K. C., & Rodgers, A. W. 1975, ApJL, 201, L71
Gillet, D., & Fokin, A. B. 2014, A&A, 565, A73
Gillet, D., Sefyani, F. L., Benhida, A., et al. 2016, A&A, 587, A134
Govea, J., Gomez, T., Preston, G. W., & Sneden, C. 2014, ApJ, 782, 59
Gratton, R. G., Bragaglia, A., Clementini, G., et al. 2004, A&A, 421, 937
Hansen, C. J., Nordström, B., Bonifacio, P., et al. 2011, A&A, 527, A65
Jayasinghe, T., Kochanek, C. S., Stanek, K. Z., et al. 2018, MNRAS, 477, 3145
Jayasinghe, T., Stanek, K. Z., Kochanek, C. S., et al. 2019, MNRAS, 485, 961
Kock, M., Kroll, S., & Schnehage, S. 1984, PhST, 8, 84
Lambert, D. L., Heath, J. E., Lemke, M., & Drake, J. 1996, ApJS, 103, 183
Lancaster, L., Koposov, S. E., Belokurov, V., Evans, N. W., & Deason, A. J.
   2019, MNRAS, 486, 378
Layden, A. C. 1994, AJ, 108, 1016
Layden, A. C., Hanson, R. B., Hawley, S. L., Klemola, A. R., & Hanley, C. J.
   1996. AJ. 112, 2110
Liu, G. C., Huang, Y., Zhang, H. W., et al. 2020, ApJS, 247, 68
Liu, S., Zhao, G., Chen, Y.-Q., Takeda, Y., & Honda, S. 2013, RAA, 13, 1307
Longmore, A. J., Fernley, J. A., & Jameson, R. F. 1986, MNRAS, 220, 279
Magurno, D., Sneden, C., Bono, G., et al. 2019, ApJ, 881, 104
Magurno, D., Sneden, C., Braga, V. F., et al. 2018, ApJ, 864, 57
Marconi, M., Coppola, G., Bono, G., et al. 2015, ApJ, 808, 50
May, M., Richter, J., & Wichelmann, J. 1974, A&AS, 18, 405
```

```
Meléndez, J., & Barbuy, B. 2009, A&A, 497, 611
Moore, C. E., Minnaert, M. G. J., & Houtgast, J. 1966, The Solar Spectrum
  2935 A to 8770 A (Washington, DC: US Government Printing Office)
Nemec, J. M., Cohen, J. G., Ripepi, V., et al. 2013, ApJ, 773, 181
Noguchi, K., Aoki, W., Kawanomoto, S., et al. 2002, PASJ, 54, 855
O'Brian, T. R., Wickliffe, M. E., Lawler, J. E., Whaling, W., & Brault, J. W.
  1991, JOSAB, 8, 1185
Pancino, E., Britavskiy, N., Romano, D., et al. 2015, MNRAS, 447, 2404
Pojmanski, G. 2002, AcA, 52, 397
Preston, G. W. 1959, ApJ, 130, 507
Ruffoni, M. P., Den Hartog, E. A., Lawler, J. E., et al. 2014, MNRAS,
  441, 3127
Saha, A. 1985, ApJ, 289, 310
Sandage, A., & Tammann, G. A. 2006, ARA&A, 44, 93
Sesar, B., Hernitschek, N., Mitrović, S., et al. 2017, AJ, 153, 204
Shappee, B. J., Prieto, J. L., Grupe, D., et al. 2014, ApJ, 788, 48
Sneden, C. 1973, ApJ, 184, 839
Sneden, C., Preston, G. W., Chadid, M., & Adamów, M. 2017, ApJ, 848, 68
Stringer, K. M., Long, J. P., Macri, L. M., et al. 2019, AJ, 158, 16
Suntzeff, N. B., Kinman, T. D., & Kraft, R. P. 1991, ApJ, 367, 528
Tody, D. 1993, in ASP Conf. Ser. 52, Astronomical Data Analysis Software
  and Systems II, ed. R. J. Hanisch, R. J. V. Brissenden, & J. Barnes (San
  Francisco, CA: ASP), 173
Torelli, M., Iannicola, G., Stetson, P. B., et al. 2019, A&A, 629, A53
Torrealba, G., Catelan, M., Drake, A. J., et al. 2015, MNRAS, 446, 2251
Wallerstein, G., Gomez, T., & Huang, W. 2012, Ap&SS, 341, 89
Wallerstein, G., Kovtyukh, V. V., & Andrievsky, S. M. 2009, ApJL, 692, L127
Weber, M., Granzer, T., & Strassmeier, K. G. 2012, Proc. SPIE, 8451, 84510K
Yanny, B., Rockosi, C., Newberg, H. J., et al. 2009, AJ, 137, 4377
Zhao, G., Zhao, Y.-H., Chu, Y.-Q., Jing, Y.-P., & Deng, L.-C. 2012, RAA,
  12, 723
Zinn, R., & West, M. J. 1984, ApJS, 55, 45
```